nature communications

Article

https://doi.org/10.1038/s41467-025-64426-7

Targeted degradation of endogenous YAP by nanobody bioPROTAC inhibits tumor progression

Received: 28 March 2024

Accepted: 12 September 2025

Published online: 23 October 2025

Check for updates

Runhua Zhou[1,2,3,9], Huifang Wang[3,9], Gui-Ming Zhang[1,2,9], Yawei Liu[4,9], Xiao-Lian Liu[1], Zhifen Li[5], Guangwei Shi[4], Junling Yuan[2], Chengming Qu[6], Yang Li[3], Liang Chen[1,2], Jingnan Huang[3], Hongchao Zhou[3], Lingyun Dai[3], Chongzhi Bai[7], Jigang Wang[2,3,8] ✉, Le Yu[2] ✉, Zhijie Li[3] ✉ & Yi-Lei Li[1] ✉

Yes-associated protein (YAP), a key effector of the Hippo pathway, regulates gene expression and promotes tumorigenesis. YAP is conventionally considered "undruggable", however, targeted protein degradation offers a promising approach to address the challenges associated with targeting this oncogenic protein. In this study, through naïve nanobody phage library screening, we identify multiple nanobodies against human YAP with high affinity and specificity. The YAP nanobody is then fused to the RING domain of RNF4, creating a bio-Proteolysis-Targeting Chimera (bioPROTAC) molecule capable of selectively targeting endogenous YAP for ubiquitin-mediated degradation. Notably, the constructed YAP bioPROTAC demonstrates significant YAP degradation and anticancer efficacy in various YAP-dependent cancers both in vitro and in vivo. Nanoparticles and adeno-associated virus (AAV) can effectively deliver the encoding gene of YAP bioPROTAC, achieving YAP degradation in tumors. Collectively, our study provides a proof-of-concept that the YAP nanobody-bioPROTAC approach can effectively degrade endogenous YAP via the ubiquitin-proteasome system, highlighting a feasible strategy for "undruggable" YAP-dependent cancers.

The Hippo pathway is a highly conserved mechanism that regulates cell and tissue growth by serving as a regulator of proliferation through the integration of various cellular cues[1]. The core kinase cascade of the Hippo pathway consists of MST1/2, MAP4Ks, and LATS1/2. The primary functional effectors of the Hippo pathway are YAP and its paralogue TAZ, which act as transcriptional regulators. The activation of the Hippo pathway leads to the phosphorylation and activation of LATS1/2 by MST1/2 or MAP4Ks. This

[1]Department of Pharmacy and Clinical Pharmacy Center, Nanfang Hospital, Southern Medical University, Guangzhou, PR China. [2]Guangdong Provincial Key Laboratory of New Drug Screening, School of Pharmaceutical Sciences, Southern Medical University, Guangzhou, PR China. [3]Guangdong Provincial Clinical Research Center for Geriatrics and Shenzhen Clinical Research Centre for Geriatrics, Shenzhen People's Hospital (The First Affiliated Hospital, Southern University of Science and Technology; The Second Clinical Medical College, Jinan University), Shenzhen, PR China. [4]Department of Neurosurgery & Medical Research Center, Shunde Hospital, Southern Medical University (The First People's Hospital of Shunde Foshan), Guangzhou, PR China. [5]School of Chemistry and Chemical Engineering, Shanxi Datong University, Datong, PR China. [6]Department of Hepatobiliary & Pancreatic Surgery, Zhongnan Hospital of Wuhan University, Wuhan, PR China. [7]Central Laboratory, Shanxi Province Hospital of Traditional Chinese Medicine, Taiyuan, PR China. [8]State Key Laboratory for Quality Ensurance and Sustainable Use of Dao-di Herbs, Artemisinin Research Center, and Institute of Chinese Materia Medica, China Academy of Chinese Medical Sciences, Beijing, PR China. [9]These authors contributed equally: Runhua Zhou, Huifang Wang, Gui-Ming Zhang, Yawei Liu.
✉e-mail: jgwang@icmm.ac.cn; yulezy@smu.edu.cn; li.zhijie@szhospital.com; lei@smu.edu.cn

phosphorylation event subsequently renders YAP/TAZ inactive through phosphorylation, resulting in their sequestration in the cytoplasm and degradation[2–4]. In their unphosphorylated form, YAP/TAZ translocate to the nucleus and interact with specific transcription factors, such as TEAD, to induce gene expression[5].

The oncogenic roles of YAP/TAZ activation or Hippo pathway inactivation have been well-documented in various types of human solid tumors[6,7]. Some tumor types display genetic alterations in the components of the Hippo pathway or its upstream modulators. This includes *NF2* mutations or deletions in mesotheliomas[8,9]; loss of LATS1/2 in cutaneous melanomas[10,11]; *GNAQ/11* mutations in uveal melanomas[12,13]. Generally, the activation of YAP/TAZ is positively associated with tumor malignancy, relapse, metastasis, decreased overall survival, and resistance to chemotherapy[14]. Therefore, YAP/TAZ signaling represents a crucial vulnerability that could potentially be targeted, offering a broad window of therapeutic efficacy for YAP- and TAZ-dependent tumors[5,14].

In the past decade, significant efforts have been devoted to identifying pharmacological approaches for inhibiting YAP/TAZ activity. Some repurposed drugs, such as the tyrosine kinase inhibitor dasatinib[15] and cholesterol-lowering statins[16], have been found to indirectly and nonspecifically inhibit YAP/TAZ, but with limited efficacy[17]. Another potential therapeutic approach involves targeting YAP/TAZ transcriptional activity through TEAD inhibition, which includes TEAD inhibitors[18], YAP/TAZ-TEAD interaction inhibitors[19,20], and small molecule-based TEAD Proteolysis Targeting Chimeras (PROTACs)[21]. TEAD PROTACs, built on reversible TEAD lipid pocket binding ligands[21] or YAP/TAZ-TEAD interaction inhibitors (disclosed in patent application WO23/031801) with E3 ligase ligands, have been shown to promote TEAD degradation and exhibit anti-proliferative effects in YAP/TAZ-dependent tumor cells. Currently, several clinical trials are underway for cancer patients based on TEAD inhibition. For instance, VT3989, a TEAD inhibitor, is in a phase I clinical trial (NCT04665206) for mesotheliomas and other tumors with *NF2* mutations. Another example is IAG933, an inhibitor of YAP/TAZ-TEAD interaction, which is being evaluated in a phase I clinical trial for tumors carrying mutations in Hippo pathway components or YAP/TAZ gene fusions (NCT04857372). Recently released phase I clinical trial results showed that VT3989 is safe and well tolerated with durable antitumor activity[22]. However, it is important to note that a limitation of this strategy is that YAP/TAZ can interact with various transcription factors or partners other than TEAD[23]. It remains uncertain whether TEAD inhibition alone is sufficient to completely block YAP/TAZ oncogenic activity. Therefore, targeting YAP/TAZ directly presents a more promising approach.

Although YAP/TAZ have been considered undruggable due to the lack of a binding pocket, their expression can be reduced at the mRNA or protein levels. Currently, a phase I clinical trial (NCT04659096) is investigating the efficacy of ION537, an anti-YAP DNA antisense oligonucleotide (ASO), in patients with advanced solid tumors. Furthermore, targeted protein degradation (TPD) is another strategy to overcome the challenges associated with the druggability of the target. The most well-known technology for TPD is PROTAC. A typical PROTAC consists of two ligands joined by an appropriate linker: one ligand binds to the protein of interest (POI), while the other recruits an E3 ubiquitin ligase. PROTACs induce proximity between the POI and the E3 ubiquitin ligase, facilitating ubiquitination of the POI and its subsequent degradation by 26S proteasome. Currently, the majority of PROTACs are small molecule-based. However, the clinical translation of small molecule PROTACs faces challenges, such as dependency on the binding pocket of the POI and off-target effects[24]. To date, there have been only two publications regarding PROTAC-induced YAP degradation, which used small molecule compounds, platanic acid[25] or a benzazepine compound (NSC682769)[26], as YAP binders. However, concerns have been raised about the specificity and degradation efficiency of these small molecule PROTACs[25,26]. Biological PROTACs (bioPROTACs), which are engineered fusion proteins comprised of a POI-binding domain (e.g., peptides and antibodies) and an E3 ligase, have emerged as a complementary strategy to small molecule PROTACs. Of note, bioPROTACs offer distinct advantages over small molecule PROTACs, including the ability to specifically bind undruggable POIs with higher affinity and lower off-target effects[24,27].

In this work, we develop a bioPROTAC capable of inducing degradation of endogenous YAP protein. This YAP bioPROTAC combines the RING domain of the ubiquitin E3 ligase RNF4 with a YAP-specific camelid nanobody, facilitating YAP destruction via the ubiquitin-proteasome system. We examine the efficacy of YAP degradation with this bioPROTAC through a lentivirus-based inducible system, nanoparticle-based delivery system, and adeno-associated virus (AAV)-based delivery system in multiple YAP-dependent cancer cells, both in vitro and in vivo. Our results demonstrate the degradation of YAP and the suppression of tumor growth, thus laying a solid foundation for targeting YAP with bioPROTACs.

Results

Screening of YAP nanobodies

The screening of nanobodies specifically targeting YAP was initiated by cloning truncated YAP (155–504 aa) and subsequently, purifying the recombinant GST fusion protein from *E. coli*. The purification process yielded a highly pure 70 kDa soluble protein (Fig. 1A). To screen nanobodies, both the purified YAP-GST and GST proteins were employed for nanobody isolation. We used a naïve alpaca nanobody phage display library with a diversity of 2×10^9, and 1×10^{11} pfu input clones were used to start the first round of panning. Three rounds of screening were performed, with one round of subtractive screening conducted prior to the third round to eliminate potential clones that bound to GST. Notably, the sub-library in the second round exhibited an enrichment of ~100-fold compared to the sub-library in the first round (3.2×10^9 pfu versus 4×10^7 pfu), indicating successful amplification and recovery of potential binders. In an effort to eliminate any GST-specific nanobodies potentially present as a result of using YAP-GST in the initial two rounds of screening, GST protein was employed as the antigen for subtractive screening during the third round, and then YAP-GST was further used for clone enrichment (Fig. 1B). Through the preliminary phage ELISA, 72 positive binders were identified out of the 192 phage clones, all of which exhibited binding to YAP (Fig. 1C, D). Sequencing analysis of these positive binders allowed for the identification of 12 nanobody sequences. Further analysis revealed two highly enriched and analogous CDR3 sequences, ALLEGTTWFSISPFDY (11/12) and ALLEGITWFSISPFDY (1/12) (Fig. 1E and Supplementary Table 1).

Characterization of YAP nanobodies

In order to evaluate the binding capability of the 12 identified nanobodies to YAP, the nanobody sequences were cloned into a pColdII vector, with the addition of an HA tag and an His tag for subsequent detection. The soluble nanobody proteins were then purified using an *E. coli* expression system and verified using HA and His tag antibodies. The molecular mass of these nanobodies was ~15 kDa (Fig. 2A). Subsequently, the binding ability of the nanobodies to YAP was confirmed using ELISA. An irrelevant nanobody (C9) was used as a negative control. Results revealed that all 12 nanobodies exhibited binding activity to YAP, while the control nanobody did not demonstrate any binding activity (Fig. 2B). Importantly, none of the nanobodies showed binding activity to GST protein (Fig. 2B). To determine the binding affinity, surface plasmon resonance (SPR) analysis was conducted. Consistent with the ELISA results, all 12 nanobodies exhibited significant binding ability, with K_D values at the nanomolar level. Notably, nanobodies E3, E4, and E8 displayed the highest affinity, with respective K_D values of 8.6 nM, 8.2 nM, and 7.6 nM and were thus prioritized for further characterization (Fig. 2C and Supplementary Fig. 1).

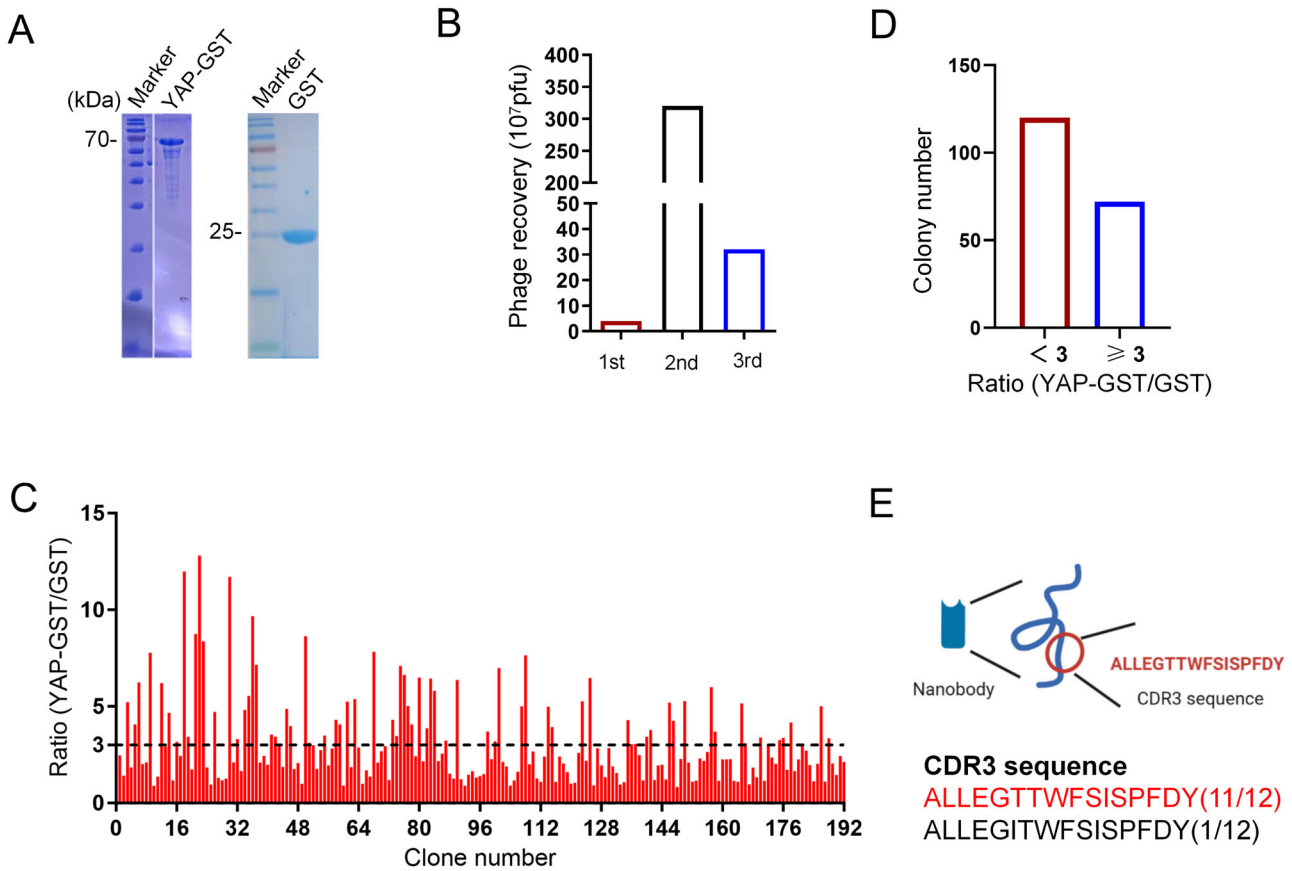

Fig. 1 | Screening of nanobodies targeting YAP proteins using a naïve phage nanobody library. A SDS-PAGE analysis of recombinant YAP-GST protein and the control GST protein. Data are representative of two independent experiments. **B** Phage titer measurement of eluates from each round of panning against YAP-GST, with negative selection against GST on the 3rd round of panning. **C**, **D** Phage ELISA experiments with 192 randomly selected clones, showing 72 clones with YAP-GST/GST OD450 value ratios >3, and 120 clones with ratios <3. **E** Two highly enriched CDR3 regions from 12 unique nanobody sequences.

To validate the ability of the identified nanobodies to bind to the natural YAP protein from cells, a HA pull-down assay followed by immunoblotting was performed. To this end, stable human uveal melanoma (UM) OMM2.3 cells and gastric cancer (GC) IM95 cells expressing doxycycline-inducible shRNAs targeting YAP were generated. The downregulation of YAP protein expression in both cell lines was effectively induced upon doxycycline treatment (Fig. 2D), and E8 nanobody was taken as an example to test the interaction with YAP protein. Of note, endogenous YAP was co-precipitated with the YAP nanobody (E8), whereas YAP deletion significantly decreased the specific interactions between YAP and E8 in both cell lines (Fig. 2D). Taken together, these results confirm the binding capability of isolated nanobodies to YAP protein, providing a solid foundation for the subsequent development of PROTAC complexes.

Construction of PROTACs targeting YAP and validation of intracellular degradation

Ubiquitin E3 ligase RNF4 contains an N-terminal domain which binds to the poly-SUMO substrate, whereas the C-terminal RING domain is responsible for ubiquitin transfer[28]. A novel degradation system for endogenous proteins, called antibody RING-mediated destruction (ARMeD), has been previously developed. In this system, the substrate recognition domain of RNF4 is replaced with a camelid nanobody, enabling the E3 ligase to target specific proteins. By linking the nanobody with two copies of RNF4 RING via a short linker, a constitutively dimeric form of RNF4 (nanobody-2 × RING) with enhanced degradation efficiency is generated. The nuclear localization signal (NLS) of RNF4 is retained, allowing efficient targeting of nuclear proteins[29]. Adopting this strategy, we constructed YAP-targeting bioPROTAC proteins: YAP-nanobody 2 × RING fusions using nanobodies E3, E4 and E8, which were selected due to their relatively high affinities to YAP (hereafter referred to as E3-2RNF4, E4-2RNF4, and E8-2RNF4, respectively).

YAP is constitutively activated in UM cells (92.1 and OMM2.3)[13], mesothelioma cells (MSTO-211H, NCI-H2373, and NCI-H2052)[8,30] and breast cancer cells (MDA-MB-231)[31] as a result of mutations in core components of the Hippo pathway or its upstream regulators (Supplementary Table 2). Importantly, these cell lines have been demonstrated to be YAP-dependent[13,18,32–34]. Additionally, we investigated multiple GC cell lines and identified AGS and IM95 as YAP-dependent (Supplementary Fig. 2). In order to assess whether the expression of YAP-nanobody bioPROTAC fusions could efficiently degrade endogenous YAP through the ubiquitin-proteasome system, we generated stable cell lines expressing doxycycline-inducible YAP-nanobody RING fusions in the aforementioned YAP-dependent cancer cells. Upon doxycycline treatment, the expression of HA-tagged irrelevant control nanobody (C3)−2RNF4 or YAP-nanobody (E3, E4, and E8)−2RNF4 was effectively induced in OMM2.3 cells. Furthermore, the ectopic expression of E3, E4, or E8-2RNF4 led to an obvious decrease in endogenous YAP levels with similar efficiency, while C3-2RNF4 failed to impact the expression of YAP in OMM2.3 cells (Supplementary Fig. 3). Given their comparable binding affinities and degradation capabilities, E8 was chosen as a representative for subsequent studies. Time course analysis of YAP degradation over a 72-h period, monitored by western blotting, revealed that E8-2RNF4 reduced YAP levels by over 80% in seven of the eight tested cell lines, except for MDA-MB-231 cells, where YAP levels were reduced by over 70% (Fig. 3A–D). The half-life ($t_{1/2}$) values, determined from the quantitative imaging data,

https://doi.org/10.1038/s41467-025-64426-7

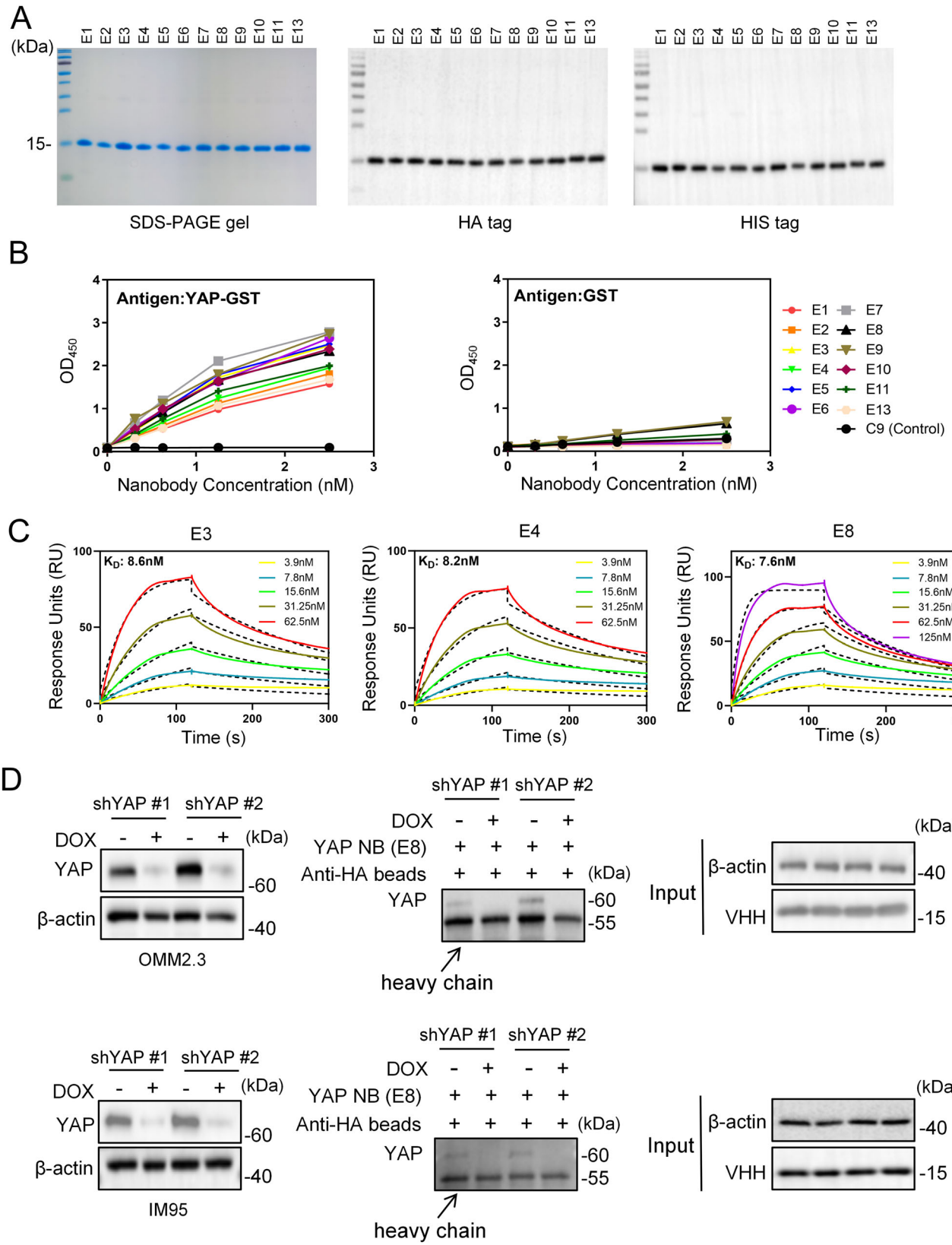

ranged from 16.8 to 36.8 h, suggesting that cell context contributes to the rate of YAP degradation. Induction of E8-2RNF4 expression was observed at 6 h post-doxycycline exposure. The delayed onset of degradation likely reflects the time taken for E8-2RNF4 to form an efficient degradation complex with YAP and for subsequent YAP ubiquitination and degradation. After doxycycline treatment, E8-2RNF4 expression increased initially and then decreased, likely due to concurrent degradation of YAP and YAP-bound E8-2RNF once the PROTAC mechanism was fully activated. Additionally, we sought to investigate the impact of YAP reduction via E8-2RNF4 on YAP activity. To do so, we performed qPCR for the classical YAP-targeted genes, including *CTGF*, *CYR61*, *CDC6*, and *FGF-1*. Consistently, doxycycline-induced expression of E8-2RNF4 significantly decreased mRNA levels of these genes (Supplementary Fig. 4). It is worth noting that with the

https://doi.org/10.1038/s41467-025-64426-7

Fig. 2 | Purification and affinity determination of YAP-specific nanobodies. **A** Purification and Western blot analysis of 12 nanobodies identified from phage ELISA. Data are representative of two independent experiments. **B** ELISA analysis evaluating the binding ability of 12 nanobodies and a negative control nanobody (C9) to YAP-GST and GST. Data from one representative experiment out of two performed is depicted. **C** Determination of nanobody E3/E4/E8 binding affinity to YAP-GST protein using Surface Plasmon Resonance (SPR). Solid lines represent the experimental sensorgrams and dashed lines indicate the fitted curves. The equilibrium dissociation constants (K_D) were measured as 8.6 nM (E3), 8.2 nM (E4), and 7.6 nM (E8), respectively. **D** Validation of the specific interaction between nanobody E8 and endogenous YAP protein through pull-down assays. YAP was down-regulated in OMM2.3 and IM95 cells using doxycycline (DOX)-inducible (Tet-on) shRNA targeting YAP. Cells were treated with or without DOX (500 ng/ml) for 48 h. Western blot analysis was performed to determine YAP protein pulled down by HA-tagged beads from cell lysates containing nanobody E8. The total protein levels were assessed using anti-actin and anti-VHH antibodies (input). Data are representative of two independent experiments.

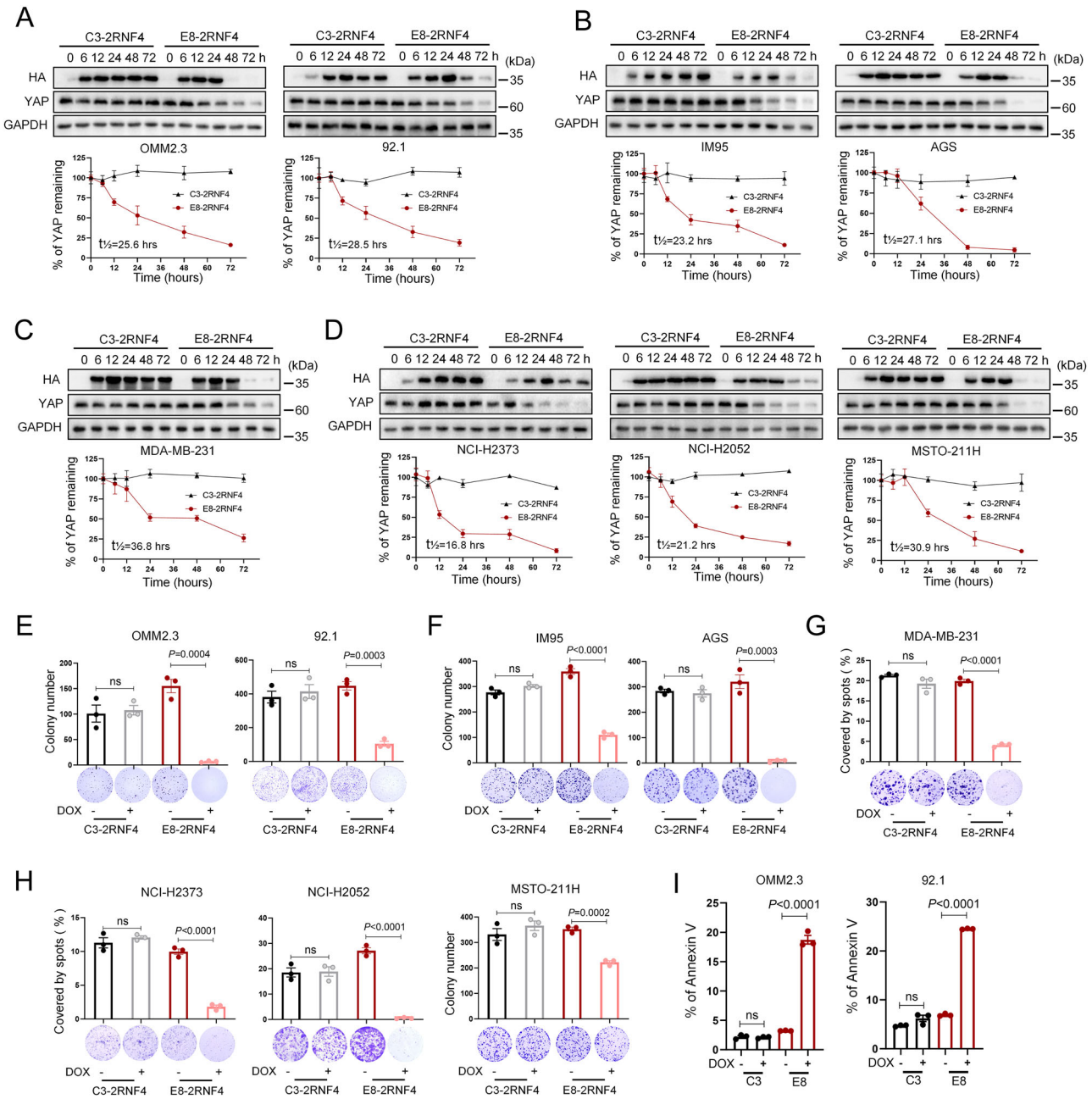

Fig. 3 | YAP Nanobody-bioPROTAC fusions induce intracellular YAP degradation and suppress tumor cell growth. Time-course experiments determining the degradation of YAP in uveal melanoma cells (OMM2.3 and 92.1) (**A**) gastric cancer cells (IM95 and AGS) (**B**) breast cancer cells (MDA-MB-231) (**C**) mesothelioma cells (NCI-H2373, NCI-H2052 and MSTO-211H) (**D**) following inducible expression of C3 or E8 nanobody-2RNF4 upon doxycycline (DOX) treatment (200 ng/ml). Quantification data are presented as mean ± SEM from three independent experiments. Colony formation assays validating the growth inhibitory effects of E8-2RNF4 on OMM2.3, 92.1 (**E**), IM95, AGS (**F**), MDA-MB-231 (**G**), NCI-H2373, NCI-H2052, MSTO-211H (**H**) cells ($n = 3$ biological replicates, mean ± SEM, two-sided Student's t-test). **I** Cell apoptosis analysis by flow cytometry after staining with Annexin V-FITC and PI. Cells stably expressing inducible E8-2RNF4 or C3-2RNF4 were treated with DOX (200 ng/ml) for 48 h ($n = 3$ biological replicates, mean ± SEM, two-sided Student's t-test, "ns" represents no significant difference). Amino acid sequences of E8-2RNF4 and C3-2RNF4 are available in Supplementary Note 1. Source data are provided as a Source Data file.

increase in doxycycline concentration, the degradation of YAP protein increased (Supplementary Fig. 5). To discern the involvement of the two main modes of ubiquitin-dependent degradation, doxycycline induction was carried out in the presence of proteasome inhibitor MG132 or autophagy inhibitor chloroquine. The data indicated that E8-2RNF4-induced YAP degradation was unaffected by chloroquine, but was blocked by MG132 in both OMM2.3 and IM95 cells (Supplementary Fig. 6). Thus, YAP-nanobody bioPROTAC fusions result in degradation of YAP primarily through the ubiquitin proteasome system.

An important question is whether YAP-nanobody bioPROTAC molecule-induced YAP reduction could inhibit YAP-dependent cancer cell growth. We observed that E8-2RNF4 significantly suppressed colony formation in all tested cell lines, while C3-2RNF4 exerted no effect (Fig. 3E–H), indicating that continuous degradation of YAP protein can profoundly suppress cell growth. Moreover, Annexin V assays revealed a significant induction of apoptosis in 92.1 and OMM2.3 cells following doxycycline-induced E8-2RNF4 expression (Fig. 3I and Supplementary Fig. 7). These data suggest the universal applicability of E8-2RNF4 in facilitating YAP degradation and thereby suppressing YAP-dependent growth and survival across various cancer cell lines.

Specificity of YAP nanobody E8

Considering the efficient YAP degradation by E8-based bioPROTAC in a panel of cancer cells, it is imperative to evaluate the target specificity of E8 to guarantee minimal off-target effects. We used YAP-null human GC cells MKN45, in which YAP expression was completely lost due to an intragenic homozygous deletion[35]. Stable MKN45 cells expressing either an empty vector (MKN45-vec) or YAP (MKN45-YAP) were generated by lentiviral transduction (Fig. 4A). In MKN45-YAP cells, the immunoblotting band probed with E8 nanobody corresponded well to the signal detected with anti-YAP antibody (Fig. 4A, B). In contrast, probing the membrane with E8 nanobody resulted in no signals in MKN45-vec cells (Fig. 4B). Dot blot analysis also revealed specific binding of E8 nanobody to YAP in MKN45-YAP cells, compared to undetectable binding in MKN45-vec cells (Fig. 4C). In-Cell ELISA data showed strong recognition of MKN45-YAP by E8 nanobody, while no signal was observed in MKN45-vec cells (Fig. 4D). Immunofluorescence staining further confirmed recognition of E8 nanobody to YAP in MKN45-YAP cells, but not in MKN45-vec cells (Fig. 4E). These results collectively validate that E8 specifically interacts with YAP. To further assess the target specificity of E8-2RNF4, we performed global proteomic analysis following doxycycline-induced expression of E8-2RNF4 in IM95 cells. This analysis confirmed that YAP was the primary protein degraded by E8-2RNF4 (Supplementary Fig. 8).

To elucidate the binding interaction between the E8 nanobody and the human YAP protein (155–504 aa), ELISA was used to investigate the binding ability of E8 to recombinant YAP fragment proteins, with GST as a negative control (Supplementary Fig. 9). Results showed that YAP (155–504 aa)-GST, YAP (1–290 aa)-GST and YAP (155–290 aa)-GST exhibited binding activity to E8, while YAP (1–154 aa)-GST, YAP (291–504 aa)-GST did not demonstrate any binding activity, similar to negative control GST (Fig. 4F). These findings suggest that YAP region spanning 155–290 aa is required for its direct interaction with E8. Next, co-immunoprecipitation (coIP) assays were conducted to investigate the interaction of E8 and YAP in HEK293T cells. Ectopically expressed HA-E8 co-precipitated with Flag-YAP (155–504 aa) (Fig. 4G). YAP deletion constructs were used to further map the interaction region (Fig. 4H). CoIP experiments revealed that E8 binds to the YAP region spanning 155–290 aa (Fig. 4I), encompassing the WW1 and WW2 domains[36]. Deletion of the WW2 domain disrupted the interaction, while deletion of the WW1 domain did not (Fig. 4J), indicating that the WW2 domain is critical for the YAP-E8 interaction, consistent with the ELISA data. SPR analysis further validated the binding specificity and affinity. The results showed that E8 binds to YAP (155–290 aa)-GST with a K_D of 9.6 nM, comparable to its affinity for YAP (155–504 aa)-GST. No binding was observed between E8 and GST alone, supporting the specificity of the interaction (Supplementary Fig. 10). Taken together, our data indicate E8 specifically interacts with WW2 domain of YAP.

Collectively, our results demonstrate the remarkable specificity of E8 nanobody to YAP protein. This attribute is crucial as it ensures the precision of E8-based bioPROTACs and minimizes off-target effects to the fullest extent.

Inducible expression of YAP bioPROTAC suppresses cancer cell dissemination in vivo

Having demonstrated the specificity, degradation efficiency, and tumor cell inhibitory efficacy of YAP bioPROTAC, we next sought to assess its anti-dissemination effects. It has been demonstrated that aberrant hyperactivation of YAP leads to an increase in cell migration[37], while knockdown of YAP using shRNAs reduces UM cell migration[13]. To investigate the impact of YAP-nanobody bioPROTAC on cell migration, transwell assays were performed in vitro. E8-2RNF4 induced by doxycycline significantly reduced migration of UM cells 92.1 and OMM2.3 (Fig. 5A). Subsequently, the effect of E8-2RNF4 on cell migration was examined in vivo using orthotopic zebrafish embryo models. The transparent nature and immune-privilege properties of zebrafish embryos allow for the direct visualization of the migration of single cancer cell, as well as metastatic intravasation and extravasation, in vivo. In the orthotopic model, fluorescently labeled UM cells (92.1 and OMM2.3) that stably expressed inducible E8-2RNF4 were injected into the posterior side of the eye in 2-day-old zebrafish embryos. Following injection, the embryos were exposed to doxycycline. Four days post-exposure, the spread of cancer cells from the engrafted eye to the head and trunk was assessed. Expression of E8-2RNF4 significantly repressed the dissemination of UM cells away from the injected eye (Fig. 5B, C). Hence, these observations support the effectiveness of YAP-nanobody bioPROTAC molecule in inhibiting the dissemination of UM cells.

Inducible expression of YAP bioPROTAC suppresses tumor growth in vivo

To investigate the potential of YAP-nanobody bioPROTAC in inhibiting tumor growth in vivo, we employed multiple immunodeficient mouse models that were xenografted with YAP-dependent cancer cells. Homozygous deletion of *NF2* in MDA-MB-231 breast cancer cells leads to YAP hyperactivation. YAP deletion using shRNAs resulted in a loss of cell viability, indicative of YAP's essential role in the survival of MDA-MB-231 cells[34]. We subcutaneously transplanted equal numbers of MDA-MB-231 cells stably expressing inducible C3-2RNF4 or E8-2RNF4 into the back flanks of nude mice and monitored their growth. Tumor growth was comparable in MDA-MB-231 cells expressing inducible C3-2RNF4, with or without doxycycline treatment. These data indicate that neither the non-targeting nanobody RING fusion nor doxycycline had any significant effect on tumor growth. In contrast, doxycycline-induced E8-2RNF4 profoundly blunted tumor growth in the xenografted mice (Fig. 6A and Supplementary Fig. 11A). Furthermore, doxycycline-induced expression of E8-2RNF4 also markedly extended the survival time of mice. However, there was no difference in survival time among the groups of C3-2RNF4 (with doxycycline), C3-2RNF4 (without doxycycline) and E8-2RNF4 (without doxycycline) (Fig. 6A, D), indicating that specific YAP degradation in MDA-MB-231 cells could significantly regress the tumor progression. Consequently, C3-2RNF4 was not used as a control in subsequent analyses due to its ineffectiveness in affecting tumor growth.

MSTO-211H mesothelioma cells, characterized by genetic deficiencies in *LATS1* and an in-frame deletion in *LATS2*, display constitutively hypophosphorylated YAP localized in the nuclei, even under YAP-inhibitory conditions[32]. Remarkably, downregulation of YAP in established MSTO-211H xenografts led to tumor regression[38]. To evaluate the effects of doxycycline-inducible YAP bioPROTAC E8-2RNF4 on tumor growth, we subcutaneously transplanted MSTO-211H

https://doi.org/10.1038/s41467-025-64426-7

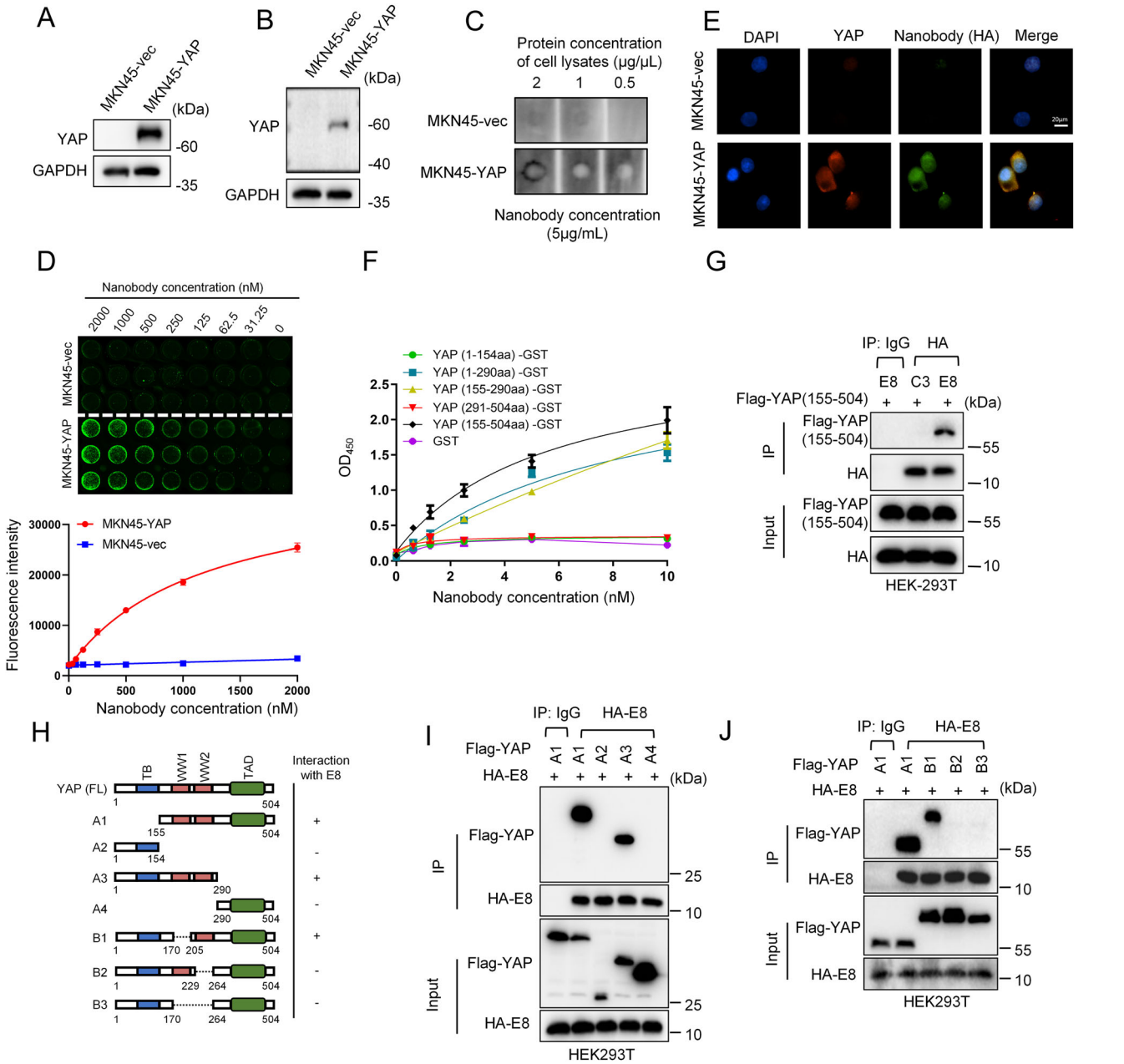

Fig. 4 | Specific binding of E8 nanobody to YAP. A Ectopic expression of YAP in MKN45 YAP-null cells was confirmed by western blot. MKN45 cells stably expressing either an empty vector (MKN45-vec) or YAP (MKN45-YAP) were generated by lentiviral infection using pLVX-empty vector or pLVX-YAP constructs. **B** Western blot analysis of E8 nanobody binding using cell lysates from MKN45-vec or MKN45-YAP. **C** Dot blot assay examining the binding of E8 to cell lysates from MKN45-vec or MKN45-YAP. **D** In-Cell ELISA analysis showing the binding of E8 nanobody to MKN45-YAP cells but not MKN45-vec cells ($n = 3$ biological replicates, mean ± SEM). **E** Immunofluorescence analysis showing specific recognition of E8 nanobody to YAP protein in MKN45-YAP cells, but not in MKN45-vec cells. Scale bar: 20 μm. **F** ELISA analysis evaluating the binding ability of E8 to recombinant YAP fragment proteins ($n = 2$ biological replicates, mean ± SEM). GST served as a negative control. Data are representative of two independent experiments. **G** Co-immunoprecipiatation (coIP) demonstrating the interaction between Flag-YAP (155-504 aa) and HA-E8. Flag-YAP was cotransfected with HA-C3 (irrelevant control nanobody) or HA-E8 in HEK293T cells. Immunoprecipitated HA-tagged proteins were analyzed for co-precipitation of Flag-YAP by Western blot. **H** Schematic diagram of YAP deletion constructs (A1/2/3/4 and B1/2/3). TB, TEAD-binding domain; TAD, C-terminal transactivation domain. **I** The YAP region spanning 155–290 aa is required for its interaction with E8. YAP deletion constructs A1/2/3/4 were cotransfected with HA-E8 into HEK293T cells, and coIP was performed to identify interacting regions. **J** WW2 domain of YAP mediates its interaction with E8. CoIP experiments, similar to (**I**), were performed using YAP deletion mutants B1/2/3. Experiments in figures (**A**–**C**, **E**, **G**, **I**, **J**) were repeated twice or more. Source data are provided as a Source Data file.

cells expressing this inducible construct into the back flanks of NCG mice. Notably, doxycycline induction significantly suppressed tumor growth and prolonged mouse survival (Fig. 6B, E, Supplementary Fig. 11B). Moreover, we investigated the impact of E8-2RNF4 on YAP-dependent IM95 GC cell growth in vivo. Despite lacking mutations in core components of the Hippo pathway or common upstream regulators (http://cellmodelpassports.sanger.ac.uk), IM95 cells still rely on YAP for proliferation (Supplementary Fig. 2). Consistently, doxycycline-induced E8-2RNF4 significantly inhibited IM95 xenograft growth and extended the survival of tumor-bearing mice (Fig. 6C, F, Supplementary Fig. 11C). UM cells harboring *GNAQ* mutations are YAP-dependent, as oncogenic *GNAQ* mutations activate YAP via both canonical and noncanonical Hippo pathways[13,39]. We subcutaneously transplanted 92.1 UM cells expressing doxycycline-inducible E8-2RNF4

https://doi.org/10.1038/s41467-025-64426-7

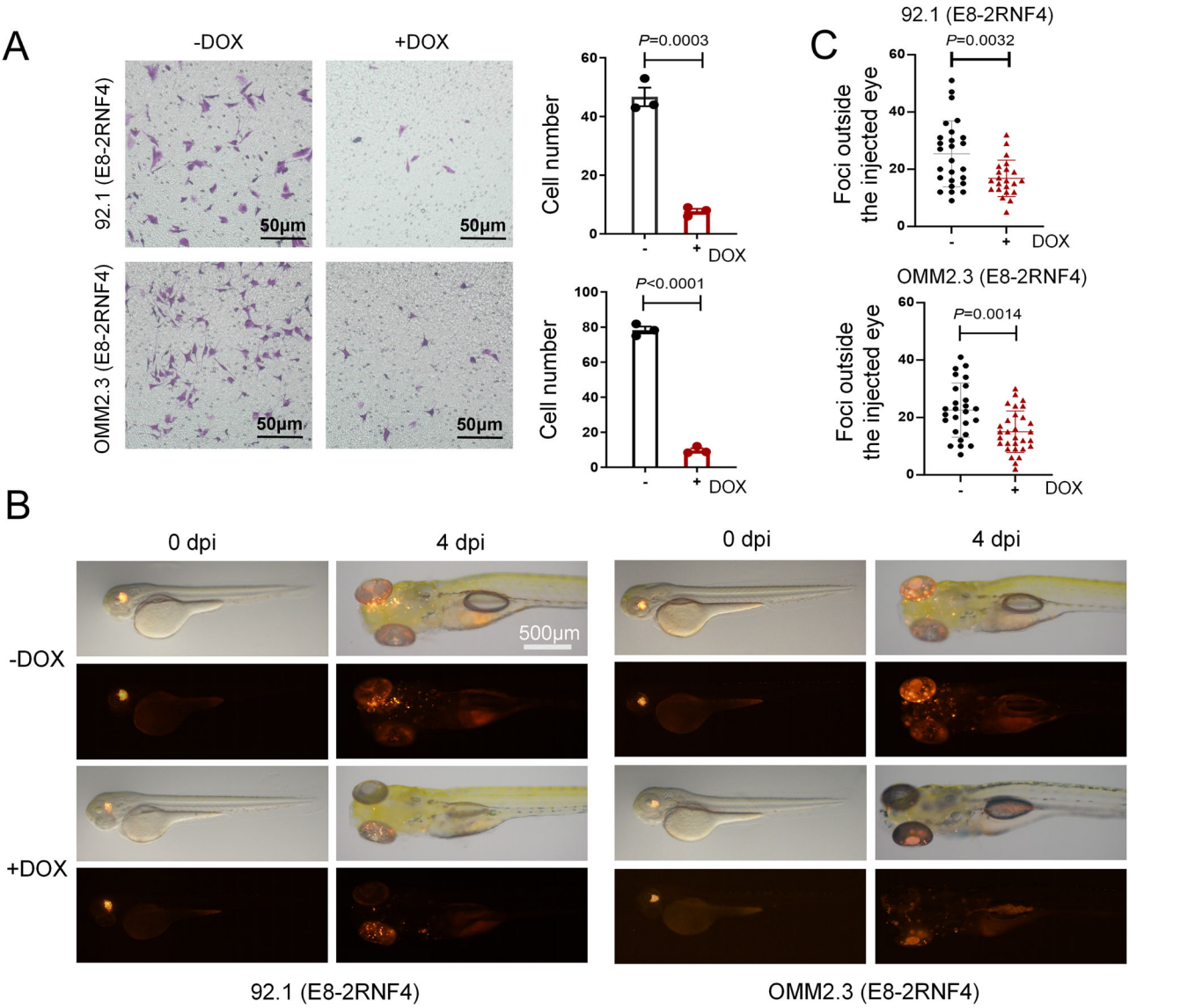

Fig. 5 | YAP bioPROTAC inhibits tumor cell migration in vitro and in vivo. **A** Representative images of migrating cells following the inducible expression of E8-2RNF4 with doxycycline (DOX). Quantitative analysis of migrating cells is shown on the right ($n = 3$, five independent fields for each membrane, mean ± SEM, two-sided Student's t-test). **B**, **C** E8-2RNF4 expression suppresses the dissemination of 92.1 and OMM2.3 cells in zebrafish embryos exposed to DOX. Quantitative analysis of tumor cell foci that migrated outside the eye is shown in (**C**) ($n = 26$ in the 92.1 control group; $n = 22$ in the 92.1 DOX-treated group; $n = 26$ in the OMM2.3 control group; $n = 30$ in the OMM2.3 DOX-treated group; mean ± SEM, two-sided Student's t-test). Source data are provided as a Source Data file.

into the back flanks of nude mice. Tumor growth was markedly retarded in mice treated with doxycycline (Fig. 6G). In line with this observation, doxycycline treatment significantly reduced tumor weights (Fig. 6H). After doxycycline treatment, tumor cells displayed induced expression of HA-tagged E8-2RNF4, accompanied by decreased nuclear expression of endogenous YAP (Fig. 6I). Furthermore, Ki-67 (a proliferation marker) expression was decreased (Fig. 6I). Taken together, these findings demonstrate that induction of YAP nanobody bioPROTAC E8-2RNF4 effectively suppresses the growth of various YAP-dependent tumors and extends survival, irrespective of the underlying YAP activation mechanisms.

Gene delivery of YAP nanobody bioPROTAC using nanoparticles realizes YAP protein degradation and suppresses tumor growth in vivo

The aforementioned doxycycline-inducible system has provided a proof of concept that YAP nanobody bioPROTAC can efficiently degrade YAP protein and inhibit YAP-dependent tumor progression. However, genetic manipulation in the cell population with doxycycline-inducible system is inapplicable for assessing YAP nanobody bioPROTAC as a feasible therapeutic strategy for cancers. To circumvent this issue, we sought to introduce plasmid DNA encoding YAP nanobody-RING fusion proteins into YAP-dependent cancer cells in xenografted mouse models using a nanoparticle delivery system. Gene therapy is a technique that employs effective nucleic acid delivery vehicles to transport DNA/RNA molecules, which typically possess strong negative charges, across native barriers such as the plasma membrane. The vehicles then release these molecules into the cytoplasm from endocytic organelles to achieve therapeutic effects. In this study, we employed polyethylenimine (PEI) as the gene carrier due to its strong electro-positivity. PEI complexes with negatively charged nucleic acids (DNA or RNA) through electrostatic interaction, facilitating gene delivery. Not only can it achieve efficient transfection in vitro, but also the nano-carrier based on PEI has been developed for tumor therapy. However, cationic polymer-based gene complexes exhibit cytotoxicity due to their strong positive charge in vivo. Hence,

https://doi.org/10.1038/s41467-025-64426-7

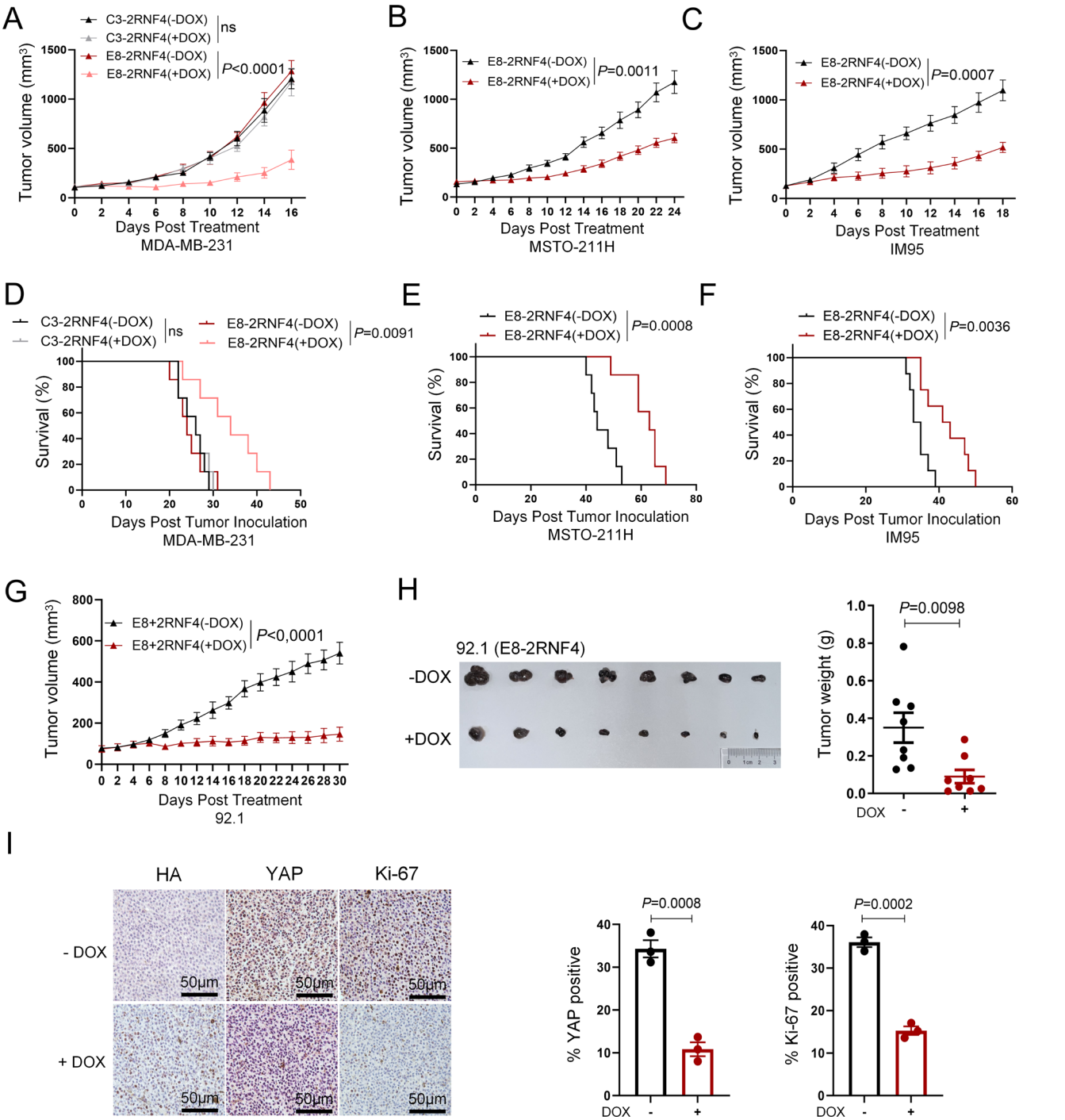

Fig. 6 | YAP nanobody bioPROTAC arrests tumor growth in vivo. A–C E8-2RNF4 inhibits tumor growth in multiple xenograft models. MDA-MB-231 (C3-2RNF4 or E8-2RNF4), MSTO-211H (E8-2RNF4), and IM95 (E8-2RNF4) cells were subcutaneously implanted into immunodeficient mice to establish multiple xenograft models. Once average tumor size reached ~100 mm^3, the animals were randomly grouped and given drinking water with/without doxycycline (DOX, 0.5 mg/ml). $n = 7$ (MDA-MB-231 and MSTO-211H), $n = 8$ (IM95). Data are mean ± SEM, two-way ANOVA with Tukey's test for multiple comparisons, "ns" represents no significant difference. **D–F** E8-2RNF4 prolongs the survival of animals in the xenografted models shown in (**A–C**). Two-sided Mantel–Cox log-rank test with Holm-Sidak correction for multiple comparisons, "ns" represents no significant difference. **G** Tumor growth curves of the 92.1 (E8-2RNF4) xenograft model. 92.1 (E8-2RNF4) cells were subcutaneously implanted into BALB/c nude mice. Once average tumor size reached ~100 mm^3, the animals were randomly grouped and given drinking water with/without DOX (0.5 mg/ml) ($n = 8$ biological replicates, mean ± SEM, two-way ANOVA). **H** Images and weights of the isolated tumor tissues from 92.1 tumor-bearing mice after euthanasia ($n = 8$ biological replicates, mean ± SEM, two-sided Student's t-test). **I** Representative immunohistochemical images for HA, YAP and Ki-67 expression in tumors from the 92.1 (E8-2RNF4) xenograft model. Quantification of YAP and Ki-67 expression is shown on the right. The DOX-treated group exhibited a notable increase in HA expression and a concurrent decrease in both YAP and Ki-67 expression ($n = 3$ biological replicates, mean ± SEM, two-sided Student's t-test). Source data are provided as a Source Data file.

we incorporated polyglutamic acid (PGA), an anionic polymer, to construct PEI/PGA/DNA mixed nanoparticles to reduce the positive charge and improve safety. In addition, previous evidence has shown that PGA promotes cell uptake of nanoparticles[40,41].

To construct nanoparticles, E8-2RNF4 was cloned into pIRES2-EGFP vector, allowing for simultaneous expression of YAP nanobody bioPROTAC fusion proteins and EGFP. EGFP was utilized to optimize transfection efficiency through fluorescence microscopy observation and flow cytometry quantification. The optimal DNA-to-PEI ratio for nanoparticle formulation was determined to be 1:3 (1 μg DNA: 3 μL PEI). Furthermore, we introduced PGA to enhance transfection efficiency while reducing charge. The nanoparticle sizes and zeta potential under various ratios were examined (Supplementary Fig. 12A, B). When the ratio of PGA to DNA was 0.5–1, the particle size uniformity improved, and the zeta potential decreased as expected. MSTO-211H cells were incubated with multiple constructed nanoparticles. The transfection efficiency of plasmids was comparable to that of the positive control PEI when the ratio of PGA to DNA was 0.5 (Supplementary Fig. 12C). Quantitative results of mean fluorescence intensity via microscopy indicated that the transfection efficiency of the group (PGA/DNA = 0.5) was close to that of the positive control PEI (Supplementary Fig. 12D). The same ratio (0.5) in IM95 even obtained better transfection efficiency than PEI (Supplementary Fig. 12E, F). Therefore, this ratio was employed for the further study. Subsequently, we assessed the impact of the optimized nanoparticles on plasmid DNA delivery and endogenous YAP degradation. The nanoparticles induced expression of HA-tagged fusion proteins and EGFP, accompanied by reduced endogenous YAP expression in MSTO-211H cells. Importantly, the effects were comparable to those observed with the positive control PEI in light of YAP degradation, although HA and EGFP levels in nanoparticle-treated cells were lower than those in PEI-treated cells (Fig. 7A).

We next sought to investigate the therapeutic potential of the protein degradation system we constructed in vivo in MSTO-211H xenografted model. Nude mice were employed to establish xenograft models with MSTO-211H cells. Nanoparticles, formulated at a PGA/DNA ratio of 0.5, were administered via peritumoral injection for treatment (20 μg DNA, 60 μL PEI, and 10 μg PGA per mouse) due to the rapid tumor progression. Results demonstrated that nanoparticles containing E8-2RNF4 plasmid significantly reduced tumor growth compared to the control group (Fig. 7B). Moreover, the treatment did not affect the body weight of mice in comparison to the control group (Fig. 7C), indicating a good biosafety in tumor-bearing mice. We noticed that C3-2RNF4 nanoparticles slightly inhibited tumor growth, possibly due to the nonspecific effect of nanoparticles. Importantly, Western blotting revealed a significant reduction in YAP expression and increased cleaved caspase 3 in tumors of E8-2RNF4 nanoparticle treated mice when compared with two control groups (Fig. 7D), whereas HA and EGFP levels as indicators for bioPROTAC protein expression and an internal control did not show significant difference between C3-2RNF and E8-2RNF4 groups (Supplementary Fig. 13), implying that the nanoparticle delivery system produces similar efficiency for both plasmid DNAs. Meanwhile, H&E staining of major vital organs from three groups did not reveal an obvious difference in morphology (Supplementary Fig. 14), indicating the good biocompatibility of these nanoparticles. Additionally, we examined the effects of E8-2RNF4 plasmid delivered by the nanoparticles on the growth of IM95 xenografts in NCG mice. We first confirmed that YAP protein was effectively degraded in IM95 cells in vitro, achieving degradation efficiency comparable to the positive control PEI (Fig. 7E). Moreover, intraperitoneal injection of nanoparticles containing E8-2RNF4 (20 μg DNA, 60 μL PEI, and 10 μg PGA per mouse) significantly suppressed IM95 tumor growth and reduced tumor weight (Fig. 7F, G) without affecting mice body weight (Supplementary Fig. 15). In contrast, nanoparticles delivering C3-2RNF4 did not exhibit antitumor activity (Supplementary Fig. 16).

Taken together, our findings demonstrate that the optimized nanoparticles efficiently deliver plasmid encoding YAP nanobody bioPROTAC E8-2RNF4 to xenografted tumor cells, leading to YAP degradation and consequently inhibiting the growth of YAP-dependent tumors.

AAV-mediated gene delivery of YAP nanobody bioPROTAC enables YAP protein degradation and tumor suppression in vivo

While the nanoparticle system has shown efficient gene delivery and YAP degradation, it is essential to explore more robust strategies to enhance the potential for translating YAP bioPROTACs. AAV has emerged as a pivotal delivery tool in gene therapy due to its minimal pathogenicity and ability to establish long-term gene expression in various tissues, with several AAV-based gene therapy products already receiving regulatory approval. Currently, numerous AAV-based gene therapies are being employed in ongoing clinical trials for a wide range of genetic and acquired diseases, including cancers[42]. To evaluate its suitability as a vector for tumor-localized delivery of YAP nanobody bioPROTACs, we generated and tested AAV9 viral vectors using the well-established strong CAG promoter to drive the expression of C3-2RNF4 and E8-2RNF4. Additionally, AAV9-YAP shRNA under the control of U6 promoter was included as a control. We first assessed whether AAV9-E8-2RNF4 infection could induce YAP degradation in IM95 cells in vitro. IM95 cells were incubated with AAV9-C3-2RNF4, AAV9-E8-2RNF4, or AAV9-YAP shRNA. Western blot analysis showed substantial induction of HA-tagged C3-2RNF4 and E8-2RNF4 expression following AAV infection. Importantly, AAV9-E8-2RNF4 dramatically reduced YAP levels, comparable to the reduction achieved by AAV9-YAP shRNA, whereas AAV9-C3-2RNF4 had no effect on YAP expression (Fig. 8A).

Next, we explored the antitumor effects of AAV9-E8-2RNF4 in the IM95 xenograft mouse model (Fig. 8B). Based on tumor growth curves and tumor weights, AAV9-E8-2RNF4 significantly inhibited tumor growth compared to the PBS control group, while AAV9-C3-2RNF4 showed no such effect. AAV9-YAP shRNA exhibited a similar antitumor effect to AAV9-E8-2RNF4 (Fig. 8C, D, Supplementary Fig. 17). Additionally, AAV9 treatment did not affect body weight compared to PBS treatment, supporting the safety of AAV9-based gene delivery in vivo (Fig. 8E). We further confirmed the expression of HA-tagged C3-2RNF4 and E8-2RNF4 in tumor tissues of mice injected with AAV9 using western blotting. Notably, AAV9-E8-2RNF4, but not AAV9-C3-2RNF4, significantly reduced YAP expression and increased cleaved caspase 3 levels. AAV9-YAP shRNA produced similar effects on YAP and cleaved caspase 3 expression (Fig. 8F). Collectively, these findings demonstrate the efficacy of AAV-mediated gene delivery of YAP nanobody bioPROTAC in promoting YAP degradation and inhibiting tumor growth.

Discussion

In this study, we identify a panel of YAP-specific nanobodies and validate their binding activity. We provide proof-of-concept that nuclear YAP can be selectively degraded by nanobody-based bioPROTACs via the ubiquitin–proteasome system. These YAP bioPROTACs demonstrate potent anticancer activity in YAP-dependent cancer cells across cell culture, zebrafish, and mouse xenograft models (Fig. 9).

YAP has been depicted as an undruggable protein owing to the absence of a binding pocket. Herein, the nanobody screening has been conducted to identify protein ligands selective for YAP with a naïve nanobody phage library. Fusion of the YAP nanobody to the RING domain of RNF4 creates a YAP-targeted bioPROTAC protein capable of inducing ubiquitin proteasome-mediated degradation of YAP. Given the fact that the transcriptional activity and oncogenic role of YAP require its nuclear localization, the NLS of RNF4 has been retained in our fusion constructs to enable effective targeting of nuclear YAP. Notably, the YAP nanobody-bioPROTAC fusions have demonstrated efficient degradation of nuclear YAP in various cancer cell lines, where

https://doi.org/10.1038/s41467-025-64426-7

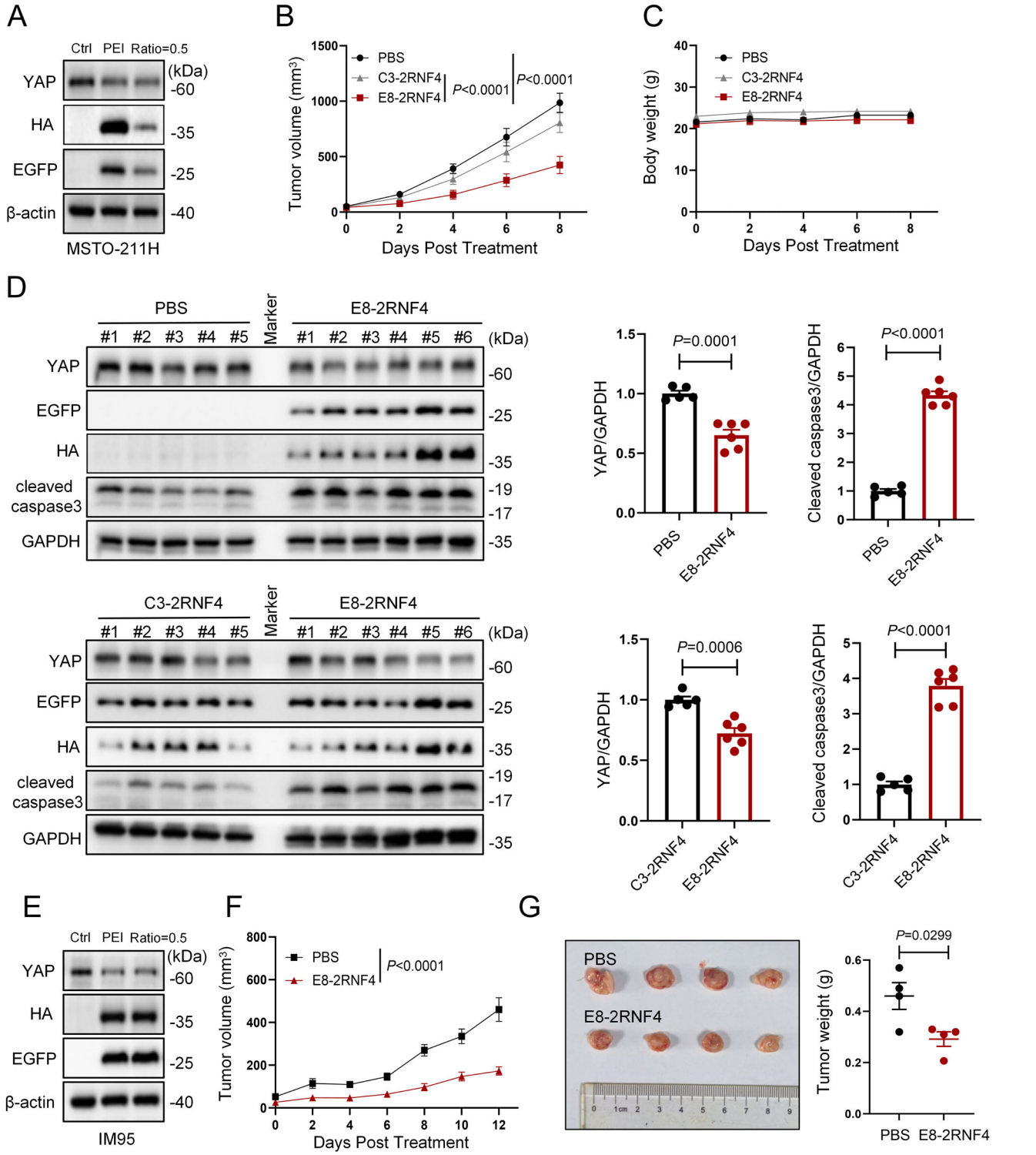

Fig. 7 | Gene delivery of YAP bioPROTAC encoding plasmid using PEI/PGA-based nanocomplexes inhibits YAP-dependent tumors. A Western blot analysis of plasmid transfection using PEI or PEI/PGA-based nanocomplexes in MSTO-211H cells. **B** Growth curves of MSTO-211H tumor xenografts. Mice were treated with various nanocomplexes (E8-2RNF4, C3-2RNF4) or PBS via peritumoral injection. $n = 5$ (PBS, C3-2RNF4); $n = 6$ (E8-2RNF4). Data are mean ± SEM, two-way ANOVA followed by Tukey's test. **C** Body weight of mice from the groups shown in (**B**). **D** Western blot analysis of tumor samples extracted from MSTO-211H-bearing mice after various treatments. E8-2RNF4 nanoparticles significantly down-regulated YAP protein levels and upregulated apoptosis indicator cleaved caspase 3 compared to both the PBS and C3-2RNF4 groups. Quantitative analysis of key indicators is presented on the right. $n = 5$ (PBS, C3-2RNF4); $n = 6$ (E8-2RNF4). Data are mean ± SEM, two-sided Student's *t*-test. **E** Western blot analysis of plasmid transfection using PEI or PEI/PGA-based nanocomplexes in IM95 cells. **F** Growth curves of IM95 tumor xenografts. Mice were treated with nanocomplexes (E8-2RNF4) or PBS via intraperitoneal injection ($n = 4$ biological replicates, mean ± SEM, two-way ANOVA). **G** Tumor images and tumor weights in mice from the groups shown in (**F**) ($n = 4$ biological replicates, mean ± SEM, two-sided Student's *t*-test). Experiments in (**A**, **E**) were repeated twice or more. Source data are provided as a Source Data file.

https://doi.org/10.1038/s41467-025-64426-7

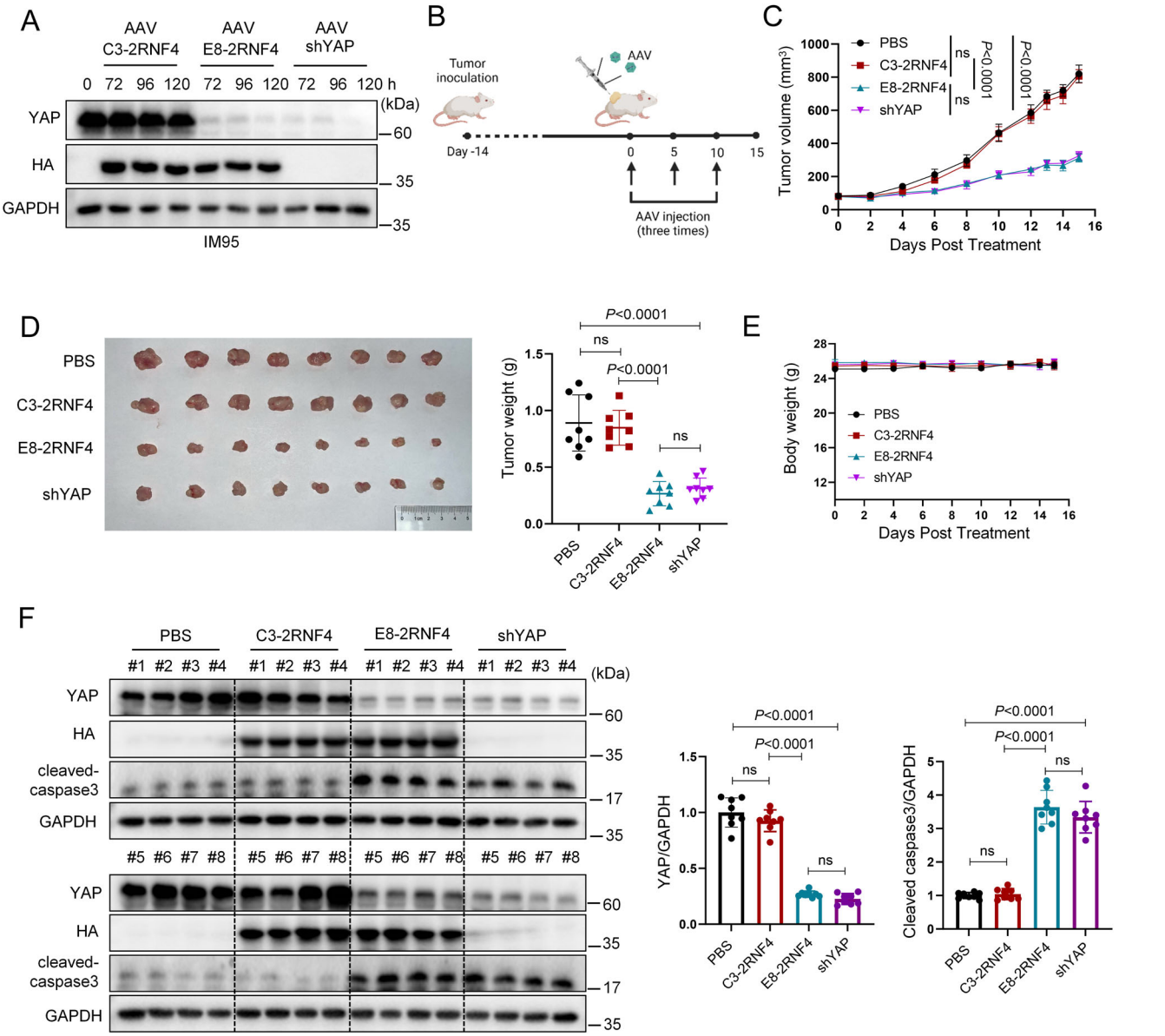

Fig. 8 | AAV9-E8-2RNF4 reduces YAP expression and suppresses tumor growth in vivo. A IM95 cells were incubated with AAV9-C3-2RNF4, AAV9-E8-2RNF4, or AAV9-YAP shRNA viral particles at a MOI of 10^5 GC per cell. YAP expression was assessed by western blot at 72, 96, and 120 hr post-transduction. Data from one representative experiment out of two performed is depicted. **B** Schematic diagram of intratumoral AAV9 treatment. Figure created in BioRender. Jiayun, C. (2025) https://BioRender.com/4b2nb1j. **C** Growth curves of IM95 tumor xenografts in mice treated with AAV9-C3-2RNF4, AAV9-E8-2RNF4, or AAV9-YAP shRNA via intratumoral injection ($n = 8$ biological replicates, mean ± SEM, two-way ANOVA followed by Tukey's test, "ns" represents no significant difference). **D** Tumor images and tumor weights from the mice shown in (**C**) (n = 8 biological replicates, mean ± SEM, one-way ANOVA followed by Tukey's test, "ns" represents no significant difference). **E** Body weights of mice during the course of treatment as shown in (**B**). **F** Western blot analysis of tumor samples extracted from IM95-bearing mice after various treatments. Quantitative analysis of YAP and cleaved caspase 3 levels is presented on the right ($n = 8$ biological replicates, mean ± SEM, one-way ANOVA followed by Tukey's test, "ns" represents no significant difference). Source data are provided as a Source Data file.

YAP is exclusively localized in the nucleus due to the mutations in *GNAQ*, *LATS1/2*, or *NF2*.

PROTACs hijack the cellular protein ubiquitination machinery to selectively degrade proteins of interest. However, the lack of specific small-molecule inhibitors for YAP poses a challenge. In contrast to small molecule ligands commonly used in PROTACs, antibodies exhibit exceptional specificity and affinity for antigens by recognizing protein surfaces. Nanobodies, derived from heavy-chain only IgG antibodies found in camelids, represent the smallest antibody entity with antigen specificity and affinity comparable to conventional full-length antibodies. Nanobodies offer favorable characteristics such as small size, high selectivity, solubility and stability, making them promising candidates for drug development. The approval of Caplacizumab in 2018 marked a significant milestone in the utilization of nanobodies for therapeutic purposes, paving the way for further advancements[43]. Recognizing the benefits of nanobodies, a growing number of studies have leveraged nanobody-based bioPROTACs to degrade previously intractable therapeutic targets, such as BCL11A[44,45], PCNA[46], and HuR[47]. Nanobody-based bioPROTACs may mitigate limitations associated with small molecule PROTACs, including off-target effects and the hook effect. A recent study has shown that through modification of immunomodulatory drugs such as thalidomide, specific degradation of endogenous proteins tagged with SD40 via prime DNA editing can be achieved[48]. This study offers

https://doi.org/10.1038/s41467-025-64426-7

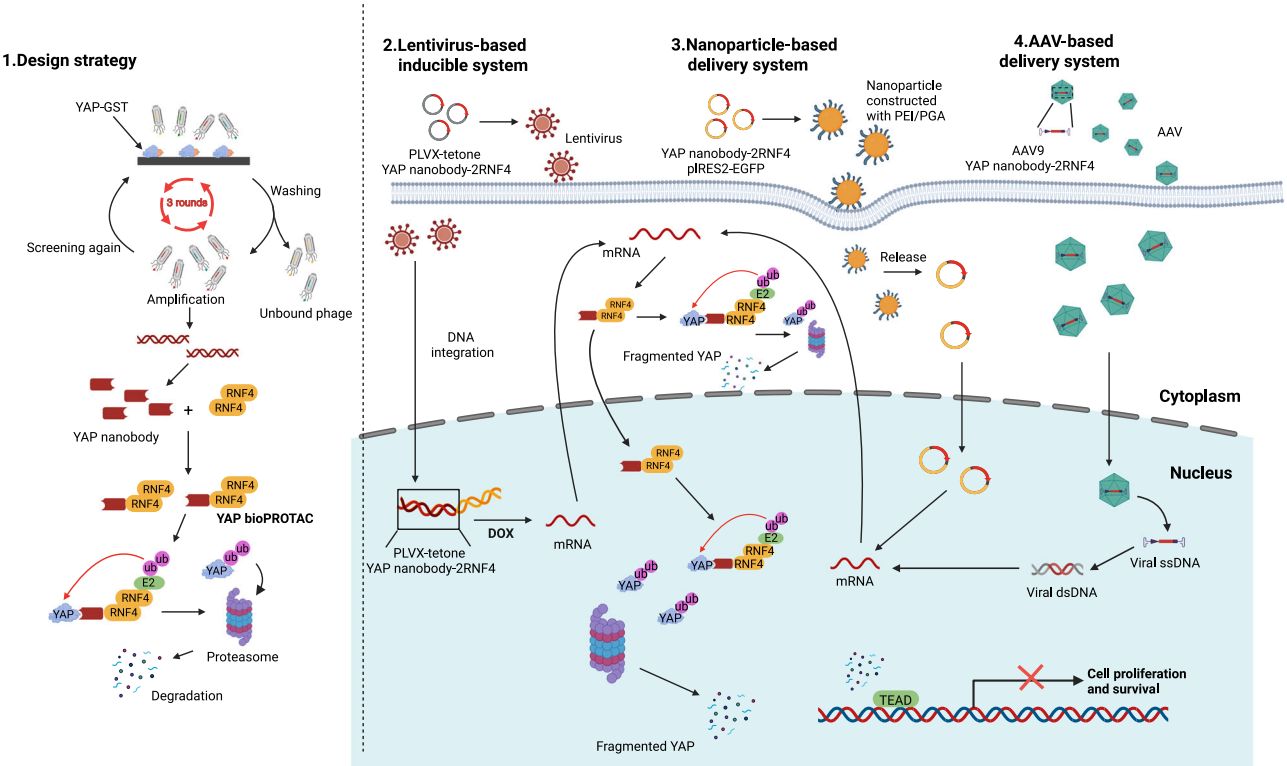

Fig. 9 | Schematic overview of the design and therapeutic application of a YAP-targeting nanobody-based bioPROTAC. (1) High-affinity nanobodies against YAP were identified by phage display screening. (2) The selected nanobodies were fused to the RING domain of RNF4 to generate a YAP bioPROTAC, expressed using a lentivirus-based doxycycline-inducible system. (3) PEI/PGA-based nanoparticles were used to encapsulate and deliver the YAP bioPROTAC gene in vivo. (4) An adeno-associated virus (AAV9) system was also employed for efficient gene delivery. The expressed bioPROTAC directs YAP for ubiquitin–proteasome degradation, leading to suppression of YAP/TEAD transcriptional activity and tumor growth. Figure created in BioRender. Jiayun, C. (2025) https://BioRender.com/4b2nb1j.

an alternative approach for developing more specific PROTACs in future. Of note, the development of a phage surface display platform to screen large libraries of nanobodies also provides a straightforward and low-cost method to obtain nanobody ligands for proteins. By utilizing this platform, we have identified multiple nanobodies specifically against YAP and characterized their binding properties. The YAP nanobodies with high affinity were then conjugated with RING domain of ubiquitin E3 ligase RNF4 to create bioPROTACs that specifically degrade endogenous YAP through proteasome-mediated degradation. As a complementary approach to RNAi-based approaches, bioPROTACs offer a way to deplete a target at the protein level, which could provide distinct benefits. RNAi-based methods typically take a long time (usually around 48 h) to achieve knockdown, making it difficult to study some biological processes[29]. In our study, E8-2RNF4 reduced YAP protein levels by ~50% at 12 h post-doxycycline induction in NCI-H2373 cells. It should be noted that this reflects both the expression kinetics of the inducible system and the degradation process. Indeed, bioPROTACs are highly modular in nature and can readily accommodate changes. It has been demonstrated that optimization of nanobody affinity, linker length/flexibility or E3 selection can accelerate the rate of degradation of targeted proteins[44,49]. Additionally, directly introducing recombinant bioPROTACs by microinjection, electroporation, or lipid nanoparticles could further hasten target protein degradation[29,50]. Therefore, while the present study serves as a proof-of-concept, we anticipate that further optimization of both construct design and delivery strategies might support more rapid YAP depletion for certain biological investigation. Another potential advantage of bioPROTAC-mediated silencing is that specific post-translational modifications can be selectively targeted[24,46]. As various YAP post-translational modifications are linked to its biological functions and pro-tumorigenic activities[51,52], the bioPROTAC approach may serve as a tool for both biological research and potential therapeutic applications.

Targeted delivery of YAP bioPROTACs to tumor cells is crucial for effective treatment. Of note, endogenous YAP has physiological roles in normal cells, such as fibroblasts and smooth muscle cells, which may lead to toxicities associated with long-term YAP inhibition[53]. Additionally, YAP has been implicated in immune regulation, raising concerns about systemic inhibition of YAP leading to immune imbalances and autoimmune and inflammatory diseases[14]. To address these concerns, it may be necessary to deliver YAP bioPROTACs specifically to cancer cells. In our studies, we observed that intraperitoneal injection of nanoparticles containing DNA encoding YAP nanobody-RING fusions could reduce YAP expression, resulting in inhibitory effects on tumor growth. This may be due to the characteristic of nanoparticles being able to accumulate in tumor tissues through enhanced permeability and retention (EPR) effect. However, active targeting of nanoparticles to tumor tissues with specificity is crucial to minimize systemic toxicity. Utilizing nanobodies targeting proteins specifically expressed on tumor cell surfaces, such as anti-HER2, has been demonstrated to enable the design of targeted nanoparticles for effective anti-tumor activity[54]. One limitation of this study lies in the specificity of YAP bioPROTAC delivery. Further investigations are warranted to develop tumor-specific delivery systems for degrading YAP proteins. Our study shows that AAV9-mediated delivery of E8-2RNF4 and YAP shRNA achieved similar and robust YAP degradation both in vitro and in vivo. Currently, accumulating preclinical studies have achieved tissue- or cell-specific AAV targeting through rational design approaches, such as insertion of functional domains into specific sites of the rAAV capsid, chemical modification of the rAAV capsid, or the use of tissue-specific promoters[42,55]. These strategies could be utilized to enable tumor-specific YAP bioPROTAC delivery.

Some human tumor types exhibit genetic alterations in components of the Hippo pathway or upstream regulators, resulting in elevated YAP activity and YAP dependency[14]. Consequently, targeting YAP represents a rational strategy for these tumors. YAP degradation by YAP nanobody-bioPROTAC fusions substantially suppresses the growth of *GNAQ*-mutated UM cells, *LATS1/2*-mutated mesothelioma cells, and *NF2*-mutated mesothelioma and breast cancer cells both in cell culture and xenografted models. Of note, YAP, TAZ, and other Hippo pathway components are rarely mutated in all other tumors, despite pervasive and widespread YAP hyperactivation. Hence, YAP activity is induced in human tumors without requiring the inactivation of Hippo pathway components[14]. Multiple mechanisms, such as epigenetic regulation, coordination with other oncogenic signaling pathways, and tumor microenvironment, may contribute to YAP activation[5,14]. We have also identified two GC cell lines (AGS and IM95), which do not carry defined mutations in Hippo pathway (http://cellmodelpassports.sanger.ac.uk) but rely on YAP, as knockdown YAP by shRNAs suppresses cell growth. In line with these findings, YAP degradation by YAP nanobody-RING fusions blunts the growth of these cell lines in vitro and in vivo. Given that a considerable proportion of YAP-dependent tumor cells lack a known Hippo pathway genetic alteration, it is crucial to identify biomarkers capable of predicting YAP dependency and sensitivity to YAP degradation. Recent studies have shown promising approaches in this regard. For example, a machine-learning framework has been developed to identify a robust, cancer type-agnostic gene expression signature to predict YAP dependency across cancers[56]. Another study has revealed that the nuclear localization of YAP appears to be a key determinant factor for the sensitivity of human HNSCC (head and neck squamous cell carcinoma) cells to YAP depletion by ASO[57].

Collectively, our study demonstrates that targeted degradation of YAP using nanobody-based bioPROTACs represents a promising therapeutic strategy for YAP-dependent cancers. This approach offers a compelling alternative for tackling YAP and other so-called "undruggable" oncogenic drivers across diverse malignancies. Beyond validating proof-of-concept efficacy, our findings highlight the broader potential of nanobody-based protein degradation platforms in expanding the druggable proteome. Further optimization of YAP bioPROTACs, including enhancement of delivery systems, anticancer efficacy, and pharmacokinetics, will be essential to maximize their therapeutic benefit and to facilitate clinical translation. Together, these efforts highlight the potential of nanobody-based bioPROTACs as a versatile and transformative modality for precision cancer therapy.

Methods

This study complies with all relevant biosafety, animal procedures, and ethical regulations. All animal experiments were approved by the Institutional Animal Care and Use Committee of Southern Medical University (Protocol Registry Number: SMUL2021069).

Cell culture

Human UM cell lines (92.1 and OMM2.3) were kindly provided by Dr. Martine Jager (Leiden University). Human GC cell line TMK-1 (JY-J1259) was from Jin Yuan Biology (Shanghai, China). Human mesothelioma cell lines MSTO-211H (CRL-2081), NCI-H2052 (CRL-5915), and NCI-H2373 (CRL-5946), human GC cell lines AGS (CRL-1739), IM95 (JCRB1075), MKN45 (JCRB0254), and N-87 (CRL-5822), human breast cancer cell line MDA-MB-231 (HTB-26), HEK293A (CRL-1573) and HEK293T (CRL-11268) were obtained from ATCC and JCRB. Human gastric epithelial cell line GES-1 (GNHu65) was from Cell Bank of Chinese Academy of Science (Shanghai, China). 92.1, OMM2.3, MSTO-211H, NCI-H2052, NCI-H2373, AGS, MKN45, N-87, TMK-1 were cultured in RPMI 1640 (Thermo Fisher); IM95, GSE-1, HEK293A, HEK293T and MDA-MB-231 were cultured in DMEM (Thermo Fisher). Media were supplemented with 10% fetal bovine serum (Gemini) and 1% penicillin-streptomycin solution (Invitrogen). Cell lines (92.1, OMM2.3, MKN45, TMK-1) were authenticated by STR. All cell lines were tested mycoplasma free prior to cell viability assays and in vivo studies.

Nanobody screening with an unimmunized naïve nanobody phage library

The nanobody screening was conducted as previously described[58,59]. Three rounds of biopanning were performed to obtain the antigen-specific VHH fragments using a naïve nanobody phage library (Naïve VHH library) prepared from PMBC RNA of more than 100 alpacas (Lama pacos) (Shenzhen KangTi Life Technology Co., Ltd., China, KTSM-CND002). Briefly, purified YAP-GST protein was coated on an immune tube at 40 μg/tube concentration overnight, followed by incubation with 3% BSA-PBS solution for 1 h at room temperature (RT). The VHH phage library was then incubated in the tube for 1 h at RT. Unbound phage clones were washed away with PBST (PBS + 0.1% Tween20). Trypsin (0.25 mg/ml) elution buffer was used to harvest the bound phages and was then neutralized with 4 mg/ml AEBSF. The eluted phage clones were subsequently amplified, rescued with M13 helper phages in *E. coli TG1* cells, precipitated with PEG-NaCl (20% PEG 800 and 2.5 M NaCl) and then resuspended in PBS. The phage library was collected and used for titration and next round screening. After two rounds of biopanning, the nanobody phage sub-library was first incubated with GST protein to eliminate the potential clones bound to GST. The collected supernatant was then applied for the third round screening against YAP-GST protein. A total of 192 phage clones were randomly picked from the eluted phage library after the third round screening and amplified for phage ELISA.

Briefly, the microtiter plates were parallelly coated with 10 μg/ml purified YAP-GST and GST proteins, respectively. The plates were blocked with a 3% BSA solution, and then phage clones were added and incubated for 1 h at RT. The plates were washed three times with PBST (PBS + 0.1% Tween20), followed by incubation with an HRP-conjugated anti-M13 monoclonal antibody (Sino Biological, Beijing, China, 11973-MM05T-H, 1:3000). The plates were then washed again with PBST and incubated with the TMB peroxidase substrate. The reaction was stopped with 1 M HCl. The absorbance was then measured at 450 nm using an automated microplate reader (LabServ K3 TOUCH, Thermo Fisher Scientific, USA). Clones showing more than 3-fold increase in absorbance value (YAP-GST vs GST) were regarded as positive. According to the ELISA data, 72 positive clones were identified, and 12 sequences were obtained after sequencing.

Protein purification

To express and purify the nanobodies, the recombinant plasmids (pCOLD II-YAP Nanobody) were transformed into BL21 (DE3) competent cells. The bacterial clones were shaken at 37 °C until reaching an optical density at 600 nm (OD600) value of 0.6. The bacteria were then induced with 0.2 mM IPTG and further incubated at 16 °C overnight. The bacteria pellets were collected by centrifugation at 8000 × *g* for 15 min at 4 °C, followed by three rounds of high-pressure crushing in lysis buffer. The supernatants were collected by centrifugation (12,000 × *g*, 45 min) and loaded onto a gravity column containing 1 mL of Ni-NTA agarose (Qiagen, Germany). Proteins with 6 × His tag were captured by Ni-NTA agarose, washed, and eluted by 250 mM Imidazole. Finally, the eluate was further purified using the AKTA Pure System (GE Healthcare Life Sciences, USA). The proteins were identified using SDS-PAGE and western blotting with 6 × His tag and HA tag antibodies. The proteins with 10% glycerol were frozen in liquid nitrogen and stored at -80 °C until needed.

Nanobody ELISA

The purified YAP-GST protein and GST protein (as a negative control) were coated on 96-well microplates (5 μg/ml) at 4 °C overnight.

The plates were then incubated with a 3% BSA/PBS solution for 1 h at RT. Serially diluted HA-tagged nanobody solutions in 1 × PBST (PBS + 0.1% Tween20) were added and incubated at RT for 1 h. After three washes, the plates were incubated with an HRP-conjugated anti-HA tag antibody (SinoBiological, China, 100028-MM10-H, 1:3000) at RT for 1 h. Subsequently, the plates were washed again with PBST and incubated with TMB peroxidase substrate (BioLegend, San Diego, CA, USA). The reaction was stopped with 1 M HCl, and absorbance was measured at 450 nm.

Affinity measurement

SPR analysis was performed on a Biacore S100 (GE Healthcare) to determine the binding affinity of nanobodies. Purified YAP-GST fusion proteins were immobilized on a CM5 sensor chip (GE Healthcare) at a concentration of 10 μg/mL, flowing at 10 μL/min for 1 min, resulting in an increase in the signal by ~300 resonance units (RU). At the same time, GST protein was captured in the flow-through pool as a reference control. Nanobodies were prepared by two-fold serial dilutions ranging from 250 nM to 3.9 nM in running buffer (1 × PBS, 0.005% Tween-20, pH 7.4). All experimental data were processed using the Biacore S100 evaluation software to calculate the association rate constant (k_{on}), dissociation rate constant (k_{off}) and equilibrium dissociation constant (K_D).

HA pull-down assay

Cell lines stably expressing doxycycline-inducible shRNAs for human YAP (OMM2.3 shYAP #1/#2, IM95 shYAP #1/#2) were treated with or without 500 ng/mL doxycycline. Cell lysates were collected after 24 h and total protein concentrations were quantified by BCA protein assay. Subsequently, 20 μg of nanobody E8 was added to each lysate, and the mixture was rotationally incubated at 4 °C for 2 h. The mixture was then divided into two portions. One portion underwent VHH examination to confirm nanobody input and β-actin detection to verify lysate concentration. The other portion was incubated with anti-HA magnetic beads (Thermo Fisher, 88837) and rotated at 4 °C for 2 h. The beads were collected, heated in loading buffer, and the bound proteins were analyzed by western blotting using a YAP antibody.

Nanoparticles (NPs) preparation

Plasmid DNAs (pIRES2-EGFP-E8-2RNF4, pIRES2-EGFP-C3-2RNF4) were purified using an endotoxin-free macroextraction kit (TIANGEN, DP117). Transfection complexes were prepared as previously described[60]. In brief, polyethylenimine (PEI)/DNA complexes were formed by mixing DNA with PEI at a 1:3 ratio (1 μg:3 μL) in HEPES buffer (pH 7.4) at RT for 20 min. Subsequently, a specific amount of PGA was introduced, vortexed, and allowed to stand for 30 min. The hydrodynamic size and zeta potential of the complexes were measured using a Nano Zetasizer. Transfection efficacy was evaluated by flow cytometry and fluorescent microscopy.

Antibodies

Antibodies against YAP (14074, 1:1000), HA-tag (3724, 1:1000), HA-tag HRP Conjugate (14031, 1:1000), Cleaved caspase 3 (9661S, 1:1000) were obtained from Cell Signaling Technology. GAPDH antibody (sc-25778, 1:10000) was purchased from Santa Cruz Biotechnology. Antibody against His-tag (ab18184, 1:1000) was purchased from Abcam. Antibody against Flag-tag (F1804, 1:1000) was from Sigma-Aldrich. Beta-actin antibody (66009-1-Ig, 1:5000) was purchased from Proteintech. Antibody against VHH (A02019, 1:1000) was purchased from Genscript. EGFP Antibody (GTX113617, 1:5000) was from GeneTex.

Immunoblot analysis, dot blot assay, and Immunoprecipitation

Immunoblotting was performed according to a standard western blot protocol (Abcam). For dot blot assay, protein samples were prepared as for western blotting and then spotted onto membranes. The membranes were then subjected to immunoblot analysis with the antibodies indicated in the figures. For immunoprecipitation, cell lysates were incubated overnight at 4 °C with primary antibodies, followed by a 2 h incubation with 10 μL magnetic protein A/G beads (Thermo Fisher, 88802). Immunocomplexes were washed three times with lysis buffer, denatured in sample buffer by boiling for 5 min, resolved on SDS-PAGE, and analyzed by Western blotting.

In-cell ELISA assay

To evaluate the binding activity of E8 nanobody to YAP, stable MKN45 cells expressing either empty vector (MKN45-vec) or YAP (MKN45-YAP) were seeded in 96-well plates and subjected to In-Cell ELISA analysis. The cells were fixed with ice-cold methanol for 10 min, followed by blocking with a 4% donkey serum solution for 1 h at RT. Serially diluted HA-tagged E8 nanobody solutions were added and incubated for 1 h at RT. After three washes with PBS, the plates were incubated with an anti-HA antibody (1:1000) for 1 h at RT. Following additional PBS washes, the plates were incubated with an Alexa Fluor 488-conjugated secondary antibody (1:2000) at RT for 1 h. After washing, the plates were imaged using the Sapphire Capture System (Sapphire, USA).

Protein extraction and digestion

IM95 cells stably expressing doxycycline-inducible E8-2RNF4 were treated with or without 200 ng/ml doxycycline for 48 h. For each condition, five biological replicates ($n = 5$) were processed. Sample preparation for proteomics analysis was performed as previously described[61]. Cells were then washed twice with pre-chilled PBS and resuspended in trifluoroacetic acid (TFA) at a 1:4 ratio (cell pellet: TFA). The suspension was incubated for 15 min, followed by microwave irradiation at 800 W for 10 seconds. A 10-fold volume of 2 M Tris base was then added to neutralize the acid. Subsequently, 10 mM tris (2-carboxyethyl) phosphine (TCEP) and 40 mM chloroacetamide (CAA) were added, and the mixture was incubated at 95 °C for 5 min for reduction and alkylation. Protein concentration was quantified using Coomassie Brilliant Blue G-250 (CBB) staining. The protein solution was first diluted with a mixture of 2 M Tris base and TFA (10:1), and further diluted with water to a final concentration of 0.2 μg/μL. Trypsin (Promega, #V5111) and LysC (Sigma, #324796-2U) were added at a 1:40 (enzyme: protein) ratio, and digestion was carried out at 37 °C for 20 h. Freshly prepared 0.1% formic acid (FA) was added to the digested samples to halt the digestion process. The resulting tryptic peptides were then desalted using Oasis HLB 96-well plates. The plates were activated with 1 mL acetonitrile, equilibrated with 1 mL 0.1% FA, then samples were loaded, washed with 0.1% FA, and eluted twice with 600 μL 60% acetonitrile in 0.1% FA. Eluates were pooled and dried using a SpeedVac. Finally, the peptides were quantified, resuspended in 2% acetonitrile and 0.1% FA, and analyzed by liquid chromatography tandem mass spectrometry (LC-MS/MS).

Proteomics data analysis

LC-MS/MS analysis and data analysis were performed as previously described[62]. LC-MS/MS analysis was conducted using an EASY-nLC 1200 system (Thermo Fisher Scientific) coupled with an Orbitrap Eclipse Tribrid mass spectrometer (Thermo Fisher Scientific) equipped with a nanoelectrospray source. For each sample, 500 ng of peptides were loaded and separated using an Acclaim PepMap 100 C18 Column (Thermo Fisher Scientific). MS1 data were acquired with a scan range of 350–1650 m/z at a resolution of 120,000 and an RF lens setting of 30%. The normalized automatic gain control (AGC) target was set to 100%, with a maximum injection time of 100 ms. For MS/MS analysis, precursors with a scan range of 400–700 m/z were isolated by the quadrupole, and 40 windows of 5 m/z were set without overlap. MS2 spectra were acquired with a scan range of 145–1450 m/z at a

resolution of 30,000, using high-energy collision-induced dissociation (HCD) with a collision energy of 30%, an RF lens setting of 30%, and a normalized AGC target of 800%, with a maximum injection time of 50 ms. A FAIMS device was set between the nanoESI source and the Orbitrap Eclipse. The FAIMS temperature was set to 100 °C, with the gas flow set to 0 and compensation voltage set to −45 V for LC-MS/MS analysis.

Proteomic data were acquired in data-independent acquisition (DIA) mode. Library-free data analysis was performed using DIA-NN (v.1.8.1), with the data searched against the canonical *Homo sapiens* protein sequences (download: 20250108, entries: 20421) downloaded from the Swissprot database and a contaminant database (contaminant entries: 244) that downloaded from https://github.com/HaoGroup-ProtContLib was used for reducing false discovery rate (FDR)[63]. The FDR was estimated using a decoy-based approach and controlled at 1% at both the peptide and protein levels. Carbamidomethylation of cysteine residues was specified as a fixed modification, while methionine oxidation and protein N-terminal acetylation were set as variable modifications; N-terminal methionine excision was also enabled. One missed cleavage was allowed, with a maximum of two variable modifications. Both MS1 and MS2 mass tolerances were set as 0 (automatic inference). The match between runs was enabled to maximize peptide identification across samples. Min peptide length set to 7, max peptide length set to 50, min precursor m/z set to 350, max precursor m/z set to 1650, min precursor charge set to 2, max precursor charge set to 7, and 1 unique peptide for protein identification. Subsequent data processing and differential analysis were conducted online using BioLadder (bioladder.cn). Protein abundance data were normalized using median normalization, and missing values were imputed using the K-nearest neighbors algorithm. Differentially expressed proteins (DEPs) were identified using a two-sided Student's *t*-test, with a threshold of $|\log2 \text{ fold change}| > 1$ and a $P < 0.05$. A volcano plot was generated online using Bioinformatics (bioinformatics.com.cn).

Colony formation assay

Cells were seeded in 12-well plates. Colonies were stained using 0.1% crystal violet and counted 10-14 days after plating.

Annexin V staining for apoptosis analysis

After treatment, cells were harvested, rinsed, and then stained with Annexin V-FITC and PI as per manufacturer protocol (Annexin V-FITC Apoptosis Detection Kit, Dojindo). Flow cytometry was used to analyze the stained cells within 1 h (BD LSRFortessa X-20).

Transwell cell migration assay

Cell migration assays were performed using BD Falcon cell culture inserts for 24-well plates with 8 μm pores filter. The bottom filter was pre-coated with fibronectin (20 μg/ml). Cells were treated with or without doxycycline (200 ng/ml, 48 h). Subsequently, 5×10^4 cells were seeded into the upper chamber of the insert in serum-free medium. The lower chamber was filled with complete medium. After 10 h, cells were fixed and stained with 0.1% crystal violet. Cells in the upper chamber were carefully removed, and cells that had migrated through the filter were assessed by photography.

Immunohistochemistry

Immunohistochemical studies were conducted on paraffin-embedded tissues. The antigen of the tissue sections was retrieved under high-pressure conditions in a 10 mM sodium citrate buffer (pH 6) for 25 min. After antigen retrieval, endogenous peroxidase was inhibited and samples were immersed in a blocking buffer (PV-6000) for 30 min. Subsequently, the samples were probed with primary antibodies against YAP (1:200), Ki67 (Cell Signaling Technology, 9449, 1:200), and HA-tag (Cell Signaling Technology, 3724, 1:500) and incubated overnight at 4 °C. Antigen-antibody complexes were detected using DAB Peroxidase Substrate Kit (ZSGB-BIO).

RNA extraction and quantitative real-time PCR with reverse transcription

Cells were harvested for RNA extraction using RNAsimple Total RNA kit (RE-03113, FOREGENE). RNA samples were reverse-transcribed to complementary DNA (cDNA) using PrimeScript RT Master Mix (RR036A, Takara). Real-time PCR was performed using GoTaq qPCR Master Mix (A6002, Promega) and the Applied LightCycler480 real-time PCR system. Relative mRNA levels were determined by normalization to endogenous *GAPDH* mRNA. Primer sequences are: *CYR61* (F: 5′-AGCCTCGCATCCTATACAACC-3′ and R: 5′-TTCTTTCACAAGGCG GCACTC-3′); *CTGF* (F: 5′-CCAATGACAACGCCTCCTG-3′ and R: 5′-TGGTGCAGCCAGAAAGCTC-3′); *CDC6* (F: 5′-CGCAAAGCACTGGATGT TT-3′ and R: 5′-CAACCCTCTTGGGAATCAGA-3′); *FGF-1* (F: 5′-GATGGC ACAGTGGATGGGAC-3′ and R: 5′-AAGCCCGTCGGTGTCCATGG-3′); *GAPDH* (F: 5′-CTCCTGCACCACCAACTGCT-3′ and R: 5′-GGGCCATCC ACAGTCTTCTG-3′).

Virus infection, exogenous gene expression and RNA interference

Lentivirus was generated using a second-generation lentiviral system in HEK293T cells. Exogenous gene expression in cell lines was mediated by lentiviral infection. Briefly, HEK293T cells were co-transfected with packaging plasmids psPAX2, pMD2.G, and a lentiviral transfer vector. The crude virus harvested from cultured supernatant was purified through centrifugation followed with 0.45 μm filtration. This was added to the target cells along with 5 μg/ml polybrene. Positive selection was performed by adding 1–2 μg/ml puromycin to the culture medium 48 h after infection.

All transient transfections were performed using PolyJet Reagent (Signagen Laboratories) according to manufacturer's protocol. HEK293T cells were transfected with (pcDNA3) Flag-YAP and (pcDNA3) HA-E8 constructs.

For lentivirus-mediated expression assay, cells stably expressing either empty vector or YAP were generated by lentiviral infection with pLVX-vector or pLVX-YAP constructs, respectively.

For AAV-mediated expression assay, cells were infected with AAV at a multiplicity of infection (MOI) of 10^5 genome copies (GC) per cell. AAV9-C3-2RNF4, AAV9-E8-2RNF4, and AAV9-YAP shRNA (#1) viral particles were produced by Genewiz (10^{13} GC/ml).

For doxycycline-inducible expression assay, cell lines were infected with lentivirus encoding all-in-one constructs with tetracycline-controlled transactivator (TetR) and target gene expression driven by tandem Tet operators. pLVX-TetOne-puro vector, which carries puromycin-resistant gene for positive selection, was used.

For the generation of cell lines stably expressing doxycycline-inducible shRNAs targeting human YAP, pLKO.1-TetOn-puro vector was used. The infection process was similar to that described above. The shRNAs used were: shYAP#1-5′-CCGGCTGGTCAGAG ATACTTCTTAACTCGAGTTAAGAAGTATCTCTGACCAGTTTTTC-3′ and shYAP#2-5′- CCGGAAGCTTTGAGTTCTGACATCCCTCGAGGGATGTCA GAACTCAAAGCTTTTTTTC-3′.

Animal work

Nude mice (6 weeks old) were purchased from Guangdong Medical Laboratory Animal Center (Guangzhou, China), while NCG mice (6 weeks old) were purchased from Gempharmatech (Jiangsu, China). Mice were housed in a Specific Pathogen-Free (SPF) grade animal facility, maintained at 22 ± 2 °C with 45-60% relative humidity with a 12-h light/dark cycle (lights on from 7:00 a.m. to 7:00 p.m.). Male mice were used for all experiments except for the MDA-MB-231 xenograft study, which used female mice. Lentivirus infected cells including MDA-MB-231 C3-2RNF4 (3×10^6), MDA-MB-231 E8-2RNF4 (3×10^6) and

92.1 E8-2RNF4 (5×10^6) were subcutaneously grafted into the right back flank of nude mice. Lentivirus infected cells MSTO-211H E8-2RNF4 (5×10^6) and IM95 E8-2RNF4 (5×10^6) were subcutaneously grafted into the right back flank of NCG mice. Once the tumors reached an appropriate size (~100 mm^3), mice were randomly assigned to either vehicle control (water) group or doxycycline treatment group. Mice in the doxycycline treatment group were fed 0.5 mg/ml doxycycline (Sigma-Aldrich) in drinking water supplemented with 5% sucrose. The doxycycline water was changed every 2 days. Tumor height and width were measured using a caliper to calculate tumor volume (= $width^2 \times height \times 0.5$). 92.1 tumor xenografts were excised, recorded, and fixed for further histological analysis. The growth curves of MDA-MB-231, MSTO-211H, IM95 tumors were terminated when a tumor volume reached 1500 mm^3. For the survival study, mice were sacrificed when tumor size reached 2000 mm^3.

For plasmid delivery therapy in vivo, animal models were constructed as described above. Once the tumors reached an appropriate size (~100 mm^3), mice were treated with plasmid-encapsulated nanoparticles (20 μg DNA, 60 μL PEI, and 10 μg PGA per mouse) via intraperitoneal injection (IM95) or peritumoral injection (MSTO-211H) every other day.

For AAV-mediated delivery therapy in vivo, the IM95 xenograft model was constructed as described above. Once the tumors reached an appropriate size (~100 mm^3), intratumoral injections of AAV9-C3-2RNF4/E8-2RNF4/YAP shRNA (5×10^{10} GC/mouse) or PBS (control group) were performed three times at intervals of 4 days.

Wild-type AB zebrafish were obtained from China Zebrafish Resource Center (Wuhan, China). Zebrafish embryos were raised at 28 °C under standard conditions. Prior to injection into the embryonic eye (48 hr post-fertilization), cells were fluorescently labeled with 5 μM CM-DiI (Thermo Fisher) for 20 min at 37 °C. Engrafted embryos were sorted to remove falsely injected embryos and then treated with or without doxycycline (1 μg/ml) and maintained at 34 °C. At 4 days post-injection (dpi), engrafted embryos were examined using an Olympus MVX10 Zoom Fluorescence Macro System Microscope. The tumor cells disseminated from the original injection site (eye) to distal regions (head, trunk, and tail) were manually counted and defined as invasive cells.

Statistical analysis

The data are presented as mean ± standard error of the mean (SEM) unless otherwise specified. Statistical analyses were conducted using GraphPad Prism software. Statistical significance was determined using two-tailed student's *t*-test for comparisons between two groups, or analysis of variance (ANOVA) for comparisons among multiple groups, as specified in the figure legends. Survival curves were evaluated using the log-rank Mantel-Cox test. A $p < 0.05$ was considered statistically significant.

Reporting summary

Further information on research design is available in the Nature Portfolio Reporting Summary linked to this article.

Data availability

The mass spectrometry proteomics data generated in this study have been deposited in the ProteomeXchange Consortium database under accession code PXD063726 via the PRIDE repository [http://proteomecentral.proteomexchange.org/cgi/GetDataset?ID=PXD063726]. The remaining data generated in this study are provided in the Article, Supplementary Information or Source Data file. Source data are provided with this paper.

References

1. Ma, S., Meng, Z., Chen, R. & Guan, K. L. The Hippo pathway: biology and pathophysiology. *Annu. Rev. Biochem.* **88**, 577–604 (2019).
2. Dong, J. et al. Elucidation of a universal size-control mechanism in Drosophila and mammals. *Cell* **130**, 1120–1133 (2007).
3. Zhao, B., Li, L., Tumaneng, K., Wang, C. Y. & Guan, K. L. A coordinated phosphorylation by Lats and CK1 regulates YAP stability through SCF(beta-TRCP). *Genes Dev.* **24**, 72–85 (2010).
4. Zhao, B. et al. Inactivation of YAP oncoprotein by the Hippo pathway is involved in cell contact inhibition and tissue growth control. *Genes Dev.* **21**, 2747–2761 (2007).
5. Franklin, J. M., Wu, Z. & Guan, K. L. Insights into recent findings and clinical application of YAP and TAZ in cancer. *Nat. Rev. Cancer* **23**, 512–525 (2023).
6. Zanconato, F., Cordenonsi, M. & Piccolo, S. YAP/TAZ at the roots of cancer. *Cancer Cell* **29**, 783–803 (2016).
7. Wang, Y. et al. Comprehensive molecular characterization of the Hippo signaling pathway in cancer. *Cell Rep.* **25**, 1304–1317 e1305 (2018).
8. Miyanaga, A. et al. Hippo pathway gene mutations in malignant mesothelioma: revealed by RNA and targeted exon sequencing. *J. Thorac. Oncol.* **10**, 844–851 (2015).
9. Offin, M. et al. Molecular characterization of peritoneal mesotheliomas. *J. Thorac. Oncol.* **17**, 455–460 (2022).
10. Furth, N. & Aylon, Y. The LATS1 and LATS2 tumor suppressors: beyond the Hippo pathway. *Cell Death Differ.* **24**, 1488–1501 (2017).
11. He, Z., Li, R. & Jiang, H. Mutations and copy number abnormalities of Hippo pathway components in human cancers. *Front. Cell Dev. Biol.* **9**, 661718 (2021).
12. Robertson, A. G. et al. Integrative analysis identifies four molecular and clinical subsets in uveal melanoma. *Cancer Cell* **32**, 204–220.e215 (2017).
13. Yu, F. X. et al. Mutant Gq/11 promote uveal melanoma tumorigenesis by activating YAP. *Cancer Cell* **25**, 822–830 (2014).
14. Piccolo, S., Panciera, T., Contessotto, P. & Cordenonsi, M. YAP/TAZ as master regulators in cancer: modulation, function and therapeutic approaches. *Nat. Cancer* **4**, 9–26 (2023).
15. Sun, J. et al. A tightly controlled Src-YAP signaling axis determines therapeutic response to dasatinib in renal cell carcinoma. *Theranostics* **8**, 3256–3267 (2018).
16. Hao, F. et al. Lipophilic statins inhibit YAP nuclear localization, co-activator activity and colony formation in pancreatic cancer cells and prevent the initial stages of pancreatic ductal adenocarcinoma in KrasG12D mice. *PLoS ONE* **14**, e0216603 (2019).
17. Ortega, A. et al. The YAP/TAZ signaling pathway in the tumor microenvironment and carcinogenesis: current knowledge and therapeutic promises. *Int. J. Mol. Sci.* **23**, 430 (2021).
18. Tang, T. T. et al. Small molecule inhibitors of TEAD Auto-palmitoylation selectively inhibit proliferation and tumor growth of NF2-deficient mesothelioma. *Mol. Cancer Ther.* **20**, 986–998 (2021).
19. Jiao, S. et al. A peptide mimicking VGLL4 function acts as a YAP antagonist therapy against gastric cancer. *Cancer Cell* **25**, 166–180 (2014).
20. Zhang, Z. et al. Structure-based design and synthesis of potent cyclic peptides inhibiting the YAP-TEAD protein-protein interaction. *ACS Med. Chem. Lett.* **5**, 993–998 (2014).
21. Pham, T. H. et al. Targeting the Hippo pathway in cancers via ubiquitination dependent TEAD degradation. *eLife* **13**, RP92450 (2024).
22. Yap, T. A. et al. First-in-class, first-in-human phase 1 trial of VT3989, an inhibitor of yes-associated protein (YAP)/transcriptional enhancer activator domain (TEAD), in patients (pts) with advanced solid tumors enriched for malignant mesothelioma and other tumors with neurofibromatosis 2 (NF2) mutations. *Cancer Res.* **83** (8_Supplement), CT006 (2023).
23. Guo, Y. et al. Context-dependent transcriptional regulations of YAP/TAZ in cancer. *Cancer Lett.* **527**, 164–173 (2022).
24. Wang, H. et al. Beyond canonical PROTAC: biological targeted protein degradation (bioTPD). *Biomater. Res.* **27**, 72 (2023).

25. Nakano, N. et al. Hybrid molecule between platanic acid and LCL-161 as a yes-associated protein degrader. *J. Biochem.* **171**, 631–640 (2022).
26. Zhou, C. et al. Exploring Degradation of Intrinsically Disordered Protein Yes-Associated Protein Induced by Proteolysis TArgeting Chimeras. *J. Med. Chem.* **67**, 15168–15198 (2024).
27. VanDyke, D., Taylor, J. D., Kaeo, K. J., Hunt, J. & Spangler, J. B. Biologics-based degraders - an expanding toolkit for targeted-protein degradation. *Curr. Opin. Biotechnol.* **78**, 102807 (2022).
28. Plechanovova, A. et al. Mechanism of ubiquitylation by dimeric RING ligase RNF4. *Nat. Struct. Mol. Biol.* **18**, 1052–1059 (2011).
29. Ibrahim, A. F. M. et al. Antibody RING-mediated destruction of endogenous proteins. *Mol. Cell* **79**, 155–166.e159 (2020).
30. Murakami, H. et al. LATS2 is a tumor suppressor gene of malignant mesothelioma. *Cancer Res.* **71**, 873–883 (2011).
31. Dupont, S. et al. Role of YAP/TAZ in mechanotransduction. *Nature* **474**, 179–183 (2011).
32. Lin, K. C. et al. Regulation of Hippo pathway transcription factor TEAD by p38 MAPK-induced cytoplasmic translocation. *Nat. Cell Biol.* **19**, 996–1002 (2017).
33. Zanconato, F. et al. Transcriptional addiction in cancer cells is mediated by YAP/TAZ through BRD4. *Nat. Med.* **24**, 1599–1610 (2018).
34. Han, H. et al. Hippo signaling dysfunction induces cancer cell addiction to YAP. *Oncogene* **37**, 6414–6424 (2018).
35. Kang, W. et al. Yes-associated protein 1 exhibits oncogenic property in gastric cancer and its nuclear accumulation associates with poor prognosis. *Clin. Cancer Res.* **17**, 2130–2139 (2011).
36. Zhao, B., Kim, J., Ye, X., Lai, Z. C. & Guan, K. L. Both TEAD-binding and WW domains are required for the growth stimulation and oncogenic transformation activity of yes-associated protein. *Cancer Res.* **69**, 1089–1098 (2009).
37. Moroishi, T. et al. A YAP/TAZ-induced feedback mechanism regulates Hippo pathway homeostasis. *Genes Dev.* **29**, 1271–1284 (2015).
38. Calvet, L. et al. YAP1 is essential for malignant mesothelioma tumor maintenance. *BMC Cancer* **22**, 639 (2022).
39. Feng, X. et al. A platform of synthetic lethal gene interaction networks reveals that the GNAQ uveal melanoma oncogene controls the Hippo pathway through FAK. *Cancer Cell* **35**, 457–472.e455 (2019).
40. Chen, L. et al. Reduction sensitive nanocarriers mPEG-g-gamma-PGA/SSBPEI@siRNA for effective targeted delivery of survivin siRNA against NSCLC. *Colloids Surf. B Biointerfaces* **193**, 111105 (2020).
41. Duan, J. et al. Targeted core-shell nanoparticles for precise CTCF gene insert in treatment of metastatic breast cancer. *Bioact. Mater.* **11**, 1–14 (2022).
42. Wang, J. H., Gessler, D. J., Zhan, W., Gallagher, T. L. & Gao, G. Adeno-associated virus as a delivery vector for gene therapy of human diseases. *Signal Transduct. Target. Ther.* **9**, 78 (2024).
43. Jin, B. K., Odongo, S., Radwanska, M. & Magez, S. Nanobodies: a review of generation, diagnostics and therapeutics. *Int. J. Mol. Sci.* **24**, 5994 (2023).
44. Shen, F. et al. A cell-permeant nanobody-based degrader that induces fetal hemoglobin. *ACS Cent. Sci.* **8**, 1695–1703 (2022).
45. Yin, M. et al. Evolution of nanobodies specific for BCL11A. *Proc. Natl. Acad. Sci. USA* **120**, e2218959120 (2023).
46. Lim, S. et al. bioPROTACs as versatile modulators of intracellular therapeutic targets including proliferating cell nuclear antigen (PCNA). *Proc. Natl. Acad. Sci. USA* **117**, 5791–5800 (2020).
47. Fletcher, A. et al. A TRIM21-based bioPROTAC highlights the therapeutic benefit of HuR degradation. *Nat. Commun.* **14**, 7093 (2023).
48. Mercer, J. A. M. et al. Continuous evolution of compact protein degradation tags regulated by selective molecular glues. *Science* **383**, eadk4422 (2024).
49. Huang, B. et al. Designed endocytosis-inducing proteins degrade targets and amplify signals. *Nature* **638**, 796–804 (2025).
50. Chan, A. et al. Lipid-mediated intracellular delivery of recombinant bioPROTACs for the rapid degradation of undruggable proteins. *Nat. Commun.* **15**, 5808 (2024).
51. Yan, F., Qian, M., He, Q., Zhu, H. & Yang, B. The posttranslational modifications of Hippo-YAP pathway in cancer. *Biochim. Biophys. Acta Gen. Subj.* **1864**, 129397 (2020).
52. Xue, X. et al. YAP ISGylation increases its stability and promotes its positive regulation on PPP by stimulating 6PGL transcription. *Cell Death Discov.* **8**, 59 (2022).
53. Sladitschek-Martens, H. L. et al. YAP/TAZ activity in stromal cells prevents ageing by controlling cGAS-STING. *Nature* **607**, 790–798 (2022).
54. Wu, W. et al. Nanobody modified high-performance AIE photosensitizer nanoparticles for precise photodynamic oral cancer therapy of patient-derived tumor xenograft. *Biomaterials* **274**, 120870 (2021).
55. Huang, Q. et al. An AAV capsid reprogrammed to bind human transferrin receptor mediates brain-wide gene delivery. *Science* **384**, 1220–1227 (2024).
56. Pham, T. H. et al. Machine-learning and chemicogenomics approach defines and predicts cross-talk of Hippo and MAPK pathways. *Cancer Discov.* **11**, 778–793 (2021).
57. Macleod, A. R. The discovery and characterization of ION-537: a next generation antisense oligonucleotide inhibitor of YAP1 in pre-clinical cancer models. *Cancer Res.* **81** (13_Supplement), ND11 (2021).
58. Jailkhani, N. et al. Noninvasive imaging of tumor progression, metastasis, and fibrosis using a nanobody targeting the extracellular matrix. *Proc. Natl. Acad. Sci. USA* **116**, 14181–14190 (2019).
59. Ma, J. et al. CDH17 nanobodies facilitate rapid imaging of gastric cancer and efficient delivery of immunotoxin. *Biomater. Res.* **26**, 64 (2022).
60. Jiang, H. et al. New path to treating pancreatic cancer: TRAIL gene delivery targeting the fibroblast-enriched tumor microenvironment. *J. Control Release* **286**, 254–263 (2018).
61. Doellinger, J., Schneider, A., Hoeller, M. & Lasch, P. Sample preparation by easy extraction and digestion (SPEED)—a universal, rapid, and detergent-free protocol for proteomics based on acid extraction. *Mol. Cell Proteom.* **19**, 209–222 (2020).
62. Hou, M. et al. Deep profiling of the proteome dynamics of pseudomonas aeruginosa reference strain PAO1 under different growth conditions. *J. Proteome Res.* **22**, 1747–1761 (2023).
63. Frankenfield, A. M., Ni, J., Ahmed, M. & Hao, L. Protein contaminants matter: building universal protein contaminant libraries for DDA and DIA proteomics. *J. Proteome Res.* **21**, 2104–2113 (2022).

Acknowledgements

This work was supported by the National Natural Science Foundation of China (82404492 (H.F.W.); 82373959 (Y.L.L.)), Guangdong Basic and Applied Basic Research Foundation (2023A1515010401 (Y.L.L.); 2023A1515110034 (H.F.W.)), Guangdong Yiyang Healthcare Charity Foundation (JZ2024071) (L.Y.), Wu Jieping Medical Foundation (320.6750.2024-6-51) (Y.L.L.), China Foundation for Youth Entrepreneurship and Employment (P24041887733) (G.M.Z.), the Innovation Team and Talents Cultivation Program of the National Administration of Traditional Chinese Medicine (ZYYCXTD-C-202002) (J.G.W.), the Science and Technology Foundation of Shenzhen (Shenzhen Clinical Medical Research Center for Geriatric Diseases) (J.G.W.), the Shenzhen Medical Research Fund (B2302051 (J.G.W.); D2403013 (Z.J.L.)), the Shenzhen Science and Technology Innovation Committee (SZSTI) (RCYX20221008092950121) (J.G.W.), the International Science and Technology Cooperation for Shenzhen Technology Innovation Plan (GJHZ20240218114508015) (Z.J.L.), the Shenzhen People's Hospital

Fund (SYWGSCGZH202405) (Z.J.L.). We thank Dr. Kun-Liang Guan (Westlake University, China) for critically discussing and revising the manuscript.

Author contributions

Y.L.L., Z.J.L., L.Y., J.G.W. conceived this project; R.H.Z., H.F.W., G.M.Z., Y.W.L., G.W.S., J.L.Y., L.C., Z.F.L., C.M.Q., Y.L., C.Z.B. completed in vitro experiments; R.H.Z., H.F.W., G.M.Z., X.L.L. performed xenograft experiments; J.N.H., H.C.Z. and L.Y.D. conducted the proteomic study and analysis; all authors contributed to data analysis and interpretation; R.H.Z., H.F.W., L.Y., Z.J.L. prepared the manuscript; all authors reviewed the manuscript; Y.L.L., Z.J.L., L.Y., J.G.W. supervised the project. All authors approved the final manuscript.

Competing interests

The authors declare no competing interests.

Additional information

Supplementary information The online version contains supplementary material available at https://doi.org/10.1038/s41467-025-64426-7.

Correspondence and requests for materials should be addressed to Jigang Wang, Le Yu, Zhijie Li or Yi-Lei Li.

Peer review information *Nature Communications* thanks Ajaybabu Pobbati, Serge Muyldermans and the other, anonymous, reviewer(s) for their contribution to the peer review of this work. A peer review file is available.